

# Polaritonic Control of Blackbody Infrared Radiative Dissociation

Enes Suyabatmaz,<sup>1</sup> Gustavo J. R. Aroeira,<sup>2</sup> and Raphael F. Ribeiro<sup>2,\*</sup>

<sup>1</sup>*Department of Physics, Emory University, Atlanta, GA, 30322*

<sup>2</sup>*Department of Chemistry, Emory University, Atlanta, GA, 30322*

(Dated: November 1, 2024)

Vibrational strong light-matter coupling offers a promising approach for controlling chemical reactivity with infrared microcavities. While recent research has examined potential mechanisms for this phenomenon, many important questions remain, including what type of reactions can be modified and to what extent this modification can be achieved. In this study, we explore the dynamics of Blackbody Infrared Radiative Dissociation (BIRD) in microcavities under weak and strong light-matter interaction regimes. Using a Master equation approach, we simulate the effects of infrared field confinement and vibrational strong coupling on BIRD rates for diatomic molecules. We present a framework explaining how infrared microcavities influence BIRD kinetics, highlighting the importance of overtone transitions in the process. Our findings outline the conditions under which significant enhancement or mild suppression of BIRD rates can be achieved, offering insights into the practical limitations and new strategies for controlling chemistry within infrared resonators.

## I Introduction

Chemical reaction control is critical in applications ranging from industrial catalysis to medicine. Conventional methods for manipulating reaction rates involve varying temperature, pressure, or catalyst composition. An unconventional approach for controlling thermal reaction kinetics has been recently reported [1–4] employing infrared (IR) microcavities [5] consisting of two moderate-quality mirrors separated by a distance  $L_C$  of the order of IR wavelengths resonant with typical molecular vibrations [6]. When a collection of molecules with sufficiently large IR oscillator strength is embedded in a resonant microcavity, vibrational strong coupling occurs as signaled by the emergence of hybrid quasiparticles (vibrational polaritons) consisting of a superposition of molecular and electromagnetic modes of the confined device [7–9]. Recent theoretical research has probed potential mechanisms for the observed polariton effects on chemical reaction rates [4, 10–19]. Still, several fundamental questions remain [20, 21], including what types of reactions can be controlled with an optical microcavity and to what extent this control can be exerted. In this study, we investigate gas-phase unimolecular dissociation activated by the absorption of microcavity blackbody infrared radiation [22] under weak and strong coupling with a suitable material.

Blackbody infrared radiative dissociation (BIRD) was proposed by Perrin in 1913 as a mechanism for gas phase unimolecular dissociation [23]. However, experimental observations in the 1920s ruled BIRD out in favor of the collisional activation mechanism [24–26]. Several decades later, the BIRD hypothesis was proven appropriate at sufficiently low pressures [27–29]. Since then, BIRD has become a valuable tool for investigating the thermal dissociation kinetics of molecular ions and clusters and has been observed in several simple and complex systems, including ion clusters, transition-metal complexes, and biopolymers [22].

The thermal radiation spectrum heavily influences BIRD rates. Given that free space and microcavity electromagnetic

density of states and thermal radiation density can be significantly different [5], microcavity BIRD is expected to proceed with different rates compared to free space BIRD. However, the extent of this change, whether suppression or enhancement can be achieved, and if strong light-matter coupling introduces new possibilities relative to the weak coupling regime remain open questions. Our study provides answers to these questions. Our quantitative analysis focuses on the dissociation of diatomic molecules induced by multiphoton or multipolariton absorption in microcavities, but several qualitative conclusions are generalizable to polyatomic systems.

The primary aim of this study is to characterize thermal radiative dissociation in microcavities. We employ a Master equation treatment to investigate this process in (i) free space, (ii) under weak coupling with a nearly empty microcavity, and (iii) under weak coupling with a polaritonic material. Our results give upper bounds for BIRD enhancement and suppression in weakly and strongly coupled microcavities and identify overtone transitions as crucial ingredients for the observed modulation of BIRD. In Sec. II, we describe our methodology, Sec. III provides the main results and related discussion, and Sec. IV summarizes our main results and conclusions.

## II Methods

### Master Equation for diatomic BIRD

Our analysis of BIRD in microcavities employs similar tools to those successfully applied to investigate this process in free space [22, 28, 30, 31]. These include a Markovian Master equation describing the time-evolution of vibrational quantum state populations with energy below the dissociation threshold defined below. Rotational degrees of freedom are ignored since they are weakly coupled to vibrational transitions, and the rotational dynamics are essentially classical at the temperatures of interest to BIRD. We also neglect Doppler and lifetime broadening throughout. The impact of nonzero vibrational linewidths on the presented results is described in **Results and Discussion**.

For the sake of simplicity, we assumed the thermalization of the background radiation is faster than all considered radiative transitions. The rate of change of the population in the  $i$ th

\* raphael.ribeiro@emory.edu

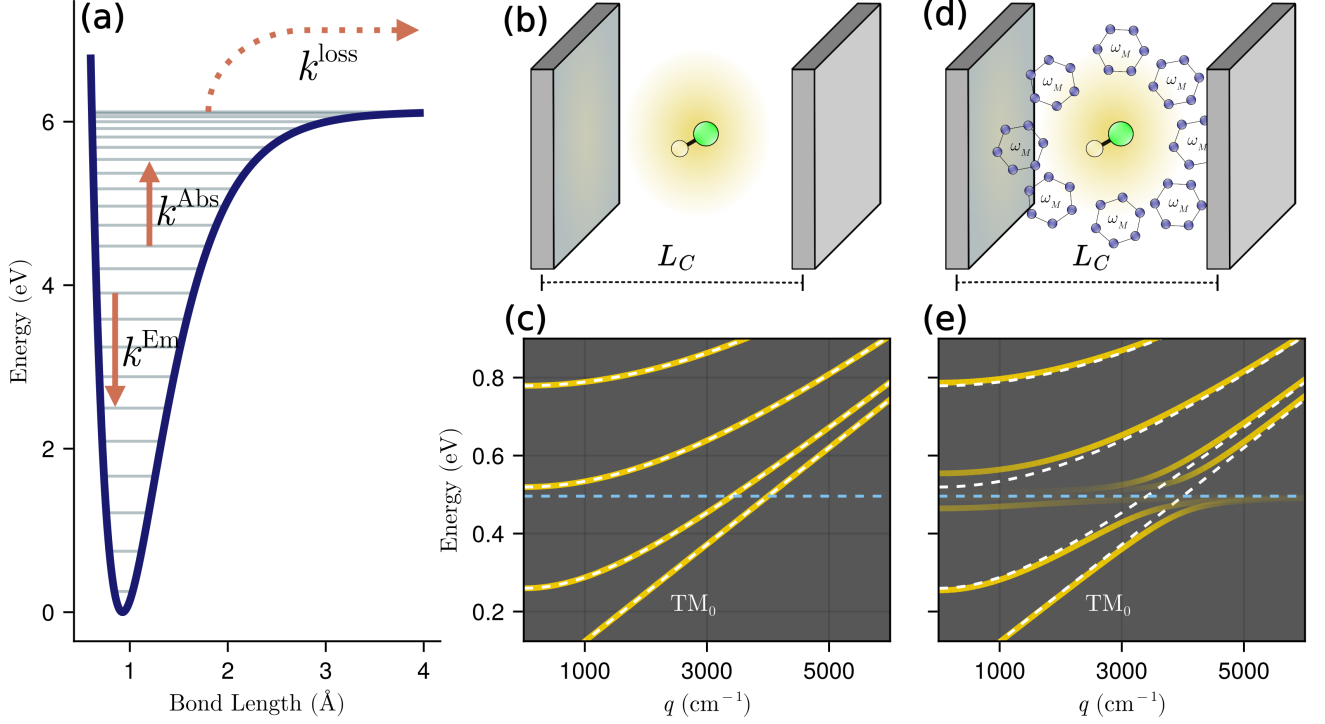


FIG. 1. (a) Illustration of the Morse potential describing the vibrational states and transitions of the HF molecule. (b) and (c): A scheme illustrating an HF molecule inside a planar cavity and its dispersion under the weak coupling regime, respectively. (d) and (e): A scheme illustrating an HF molecule inside a planar cavity with the host material strongly coupled to the cavity and the dispersion of polariton states, respectively.

vibrational state ( $N_i$ ) is given by

$$\frac{dN_i(t)}{dt} = \sum_{j \neq i}^{i_{\max}} [k_{ij}N_j(t) - k_{ji}N_i(t)] - k_{\text{loss}}N_i(t)\delta_{i,i_{\max}}, \quad (1)$$

where  $k_{ij}$  denotes rate of absorption when  $i > j$  and emission when  $i < j$  and  $i_{\max}$  is the highest energy bound state (Fig. 1a). This state is only loosely bound and is assumed to undergo irreversible dissociation at a rate  $k_{\text{loss}} \gg k_{ij} \forall i, j$ . Equation 1 can be written in matrix notation as

$$\frac{d[\mathbf{N}]}{dt} = -\mathbf{J} \cdot [\mathbf{N}], \quad (2)$$

where  $\mathbf{N}$  is a column vector containing the vibrational populations and  $\mathbf{J}$  is the transition matrix. The lowest eigenvalue  $\lambda_0$  of  $\mathbf{J}$  is the rate constant of the unimolecular reaction [32, 33] of the described mechanism. Note that this mechanism does not consider dissociation from intermediate vibrational levels ( $\nu < i_{\max}$ ). Thus, our results are expected to be valid for BIRD promoted by multiphoton dissociation through a particular doorway state, which is the highest-energy bound state in our case.

### Radiative transition rates

Assuming the molecular system that undergoes BIRD is weakly coupled to the radiation field, the transition rates  $k_{ij}$

can be obtained from perturbation theory (Fermi's Golden Rule [34, 35]) and written in terms of Einstein coefficients in free space [36, 37] and their generalizations in a weakly coupled and polaritonic microcavity. Rotational dynamics is much faster than thermal infrared radiative transition, so we employ isotropically averaged radiative rates in the long-wavelength limit (electrical dipole approximation) throughout this work.

In free space, the spontaneous emission rate is given by the Einstein  $A$  coefficient [36, 37]. In the case where spontaneous emission induces the  $i \rightarrow j$  transition with  $i > j$  this coefficient is given by

$$k_{ij}^{\text{SpEm}} = A_{ij} = \frac{\omega_{ij} |\mu_{ij}|^2 \pi}{3\epsilon_0 \hbar} D_0(\omega_{ij}), \quad (3)$$

where  $\epsilon_0$  and  $\hbar$  are the vacuum electrical permittivity and reduced Planck's constant, respectively,  $\omega_{ij} = (E_i - E_j)/\hbar$  is the transition frequency,  $\mu_{ij}$  is the corresponding transition dipole moment and  $D_0(\omega) = \omega^2/\pi^2 c^3$  is the free-space radiative density of states (DOS). The Einstein  $B$  coefficient associated with stimulated emission and absorption processes involving states  $i$  and  $j$  is given by  $B_{ij} = \pi |\mu_{ij}|^2 / (3\epsilon_0 \hbar^2)$ . The corresponding thermal stimulated emission and absorption rate constants are given by

$$k_{ij}^{\text{Abs}}(T) = k_{ij}^{\text{StEm}}(T) = B_{ij} \rho_0(\omega_{ij}, T), \quad (4)$$

where  $\rho_0(\omega, T)$  is the free space blackbody radiation energy density

$$\rho_0(\omega, T) = \hbar\omega n_{\text{BE}}(\omega, T)D_0(\omega), \quad (5)$$

and  $n_{\text{BE}}(\omega, T)$  is the Bose-Einstein distribution thermal occupation number  $n_{\text{BE}}(\omega, T) = 1/[\exp(\hbar\omega/k_B T) - 1]$ [38] and  $k_B$  is the Boltzmann constant.

The final pieces necessary to compute the rate constants above are the transition dipole matrix  $\mu_{ij}$  and the frequencies  $\omega_{ij}$ . We estimate the latter assuming the electronic ground-state potential energy curve of the examined diatomic molecules is given by the Morse potential [Fig. 1(a)][39]. The bound wave functions associated with the Morse potential are also employed in the computation of the vibrational transition dipole moments  $\mu_{ij}$  via

$$\mu_{ij} = \int \psi_i^*(r)\mu(r)\psi_j(r)dr, \quad (6)$$

where  $\psi_i(r)$  represents the  $i$ th vibrational level wave function, and the dipole function  $\mu(r)$  models the nonlinear change in the (electronic ground-state) molecular electrical dipole with the bond length  $r$  [40].

We investigated the IR radiative dissociation of hydrogen fluoride, HF, and lithium hydride, LiH. The employed dipole function  $\mu(r)$  for HF is  $\mu(r) = \mu_0 r e^{-\zeta r^4}$ , where  $\mu_0 = 0.45414e$  and  $\zeta = 0.081616 \text{ \AA}^{-4}$  were obtained from previous work on laser-induced HF dissociation[41]. The LiH dipole function was interpolated from *ab initio* quantum chemical computations (CCSD(T)/aug-cc-pVTZ, see Supplementary Information for further details). Morse potential parameters include the equilibrium bond length ( $r_e$ ), electronic ground-state dissociation energy ( $D_e$ ), and harmonic frequency ( $\omega_e$ ) of each molecule and are listed in Table I.

TABLE I. Parameters used for Morse potential of HF [41–44] and LiH [45].

Constant	HF	LiH
$D_e$ (eV)	6.123	2.641
$r_e$ (Å)	0.926	1.595
$\nu_e$ (cm <sup>-1</sup> )	4138	1405
$\nu_e \chi_e$ (cm <sup>-1</sup> )	86.7	28.3
$m_r$ (a.u)	0.95	0.88

The examined dissociation processes (via the most energetic bound state) have reduced room temperature rates relative to typical BIRD experiments involving polyatomic ions [22, 27, 29, 46] due to the relatively high stability and restricted number of state-space pathways available for diatomic dissociation proceeding via the highest energy level. This feature motivated our choice of examining diatomic BIRD at temperatures  $T = \mathcal{O}(\hbar\omega_e/k_B)$ , an order of magnitude greater than room temperature. The SI shows that the trends discussed below hold for a wide interval of temperatures. Despite their different energetics, microcavity effects on HF and LiH BIRD yield the same qualitative behavior.

The transition rates  $k_{ij}$  are proportional to the electromagnetic density of states  $D(\omega)$ , suggesting BIRD rates can be

controlled by placing the reactive molecule inside a microcavity. To examine this scenario, we adapt the free space formalism described above to arbitrary photonic devices by replacing  $D_0(\omega)$  in Eqs. 3 and 5 with the appropriate DOS for a weakly coupled microcavity  $D_C(\omega)$ .

In a planar empty Fabry-Perot microcavity composed of two parallel mirrors (with unit reflectivity for simplicity) separated by a distance  $L_C$ , [Fig. 1(b)], the frequencies of the electromagnetic modes are given by

$$\omega_C(m, \mathbf{q}) = c\sqrt{q^2 + \frac{m^2\pi^2}{L_C^2}}, \quad (7)$$

where  $\mathbf{q} = (q_x, q_y) \in \mathbb{R}^2$  is the in-plane projection of the mode wave vector,  $q^2 = q_x^2 + q_y^2$ , and  $m$  is an integer quantum number that identifies the longitudinal wave vector  $k_z = m\pi/L_C$  and thus the photonic energy bands in Fig. 1(c). For transverse-magnetic (TM) modes  $m = 0, 1, 2, \dots$  whereas  $m = 1, 2, 3, \dots$  for transverse-electric (TE) modes [47, 48]. Including the TM<sub>0</sub> mode here is crucial, as otherwise, transitions with energy below the cavity cutoff would be impossible.

Using Eq. 7, it can be shown (see Supporting Information) that the spatially-averaged electromagnetic DOS inside a microcavity in the weak coupling regime can be expressed by [49]

$$D_C(\omega) = \frac{\omega}{\pi c^2 L_C} \left[ \frac{\omega L_C}{\pi c} \right] + \frac{\omega}{2\pi c^2 L_C}, \quad (8)$$

where  $\lfloor x \rfloor$  denotes the floor function.

Lastly, we considered the BIRD scenario in which the diatomic interacts weakly with the electromagnetic component of polariton modes emergent from vibrational strong coupling between the microcavity modes and a material system (solid-state or molecular ensemble) with sufficiently large IR oscillator strength. We emphasize this material system does not undergo BIRD; its role is to generate polariton normal-modes with a *tunable* density of states and thermal energy density, as shown in Figs. 1(d) and (e). The formalism discussed above for BIRD in a weakly coupled microcavity can be straightforwardly adapted to model polariton-mediated BIRD (see SI) by replacing the photon density of states  $D_0(\omega)$  with the *photon-weighted polariton density of states*  $D_P(\omega)$ .

The Hamiltonian of the strongly coupled molecular subsystem and the microcavity is given in the Power-Zienau-Woolley (dipole) gauge [50, 51]

$$H = H_{\text{SM}} + H_L + H_{\text{INT}}, \quad (9)$$

where the interaction  $H_{\text{INT}}$  is given by

$$H_{\text{INT}} = \frac{1}{\epsilon_0} \int \left[ -\mathbf{D}(\mathbf{r}) \cdot \mathbf{P}(\mathbf{r}) + \frac{1}{2} \mathbf{P}^2(\mathbf{r}) \right] d^3\mathbf{r}, \quad (10)$$

where  $\mathbf{P}(\mathbf{r})$  is the matter polarization density and  $\mathbf{D}(\mathbf{r})$  is the electrical displacement field [52, 53]. The pure matter and bare electromagnetic Hamiltonians  $H_{\text{SM}}$  and  $H_L$  generate the dynamics of a collection of free harmonic oscillators corresponding to isotropic uniformly distributed matter vibrations

(e.g., from a dispersionless paraelectric material [54, 55]) and the planar microcavity modes with frequency-momentum dispersion given by Eq. 7. Assuming a strongly coupled 3D isotropic material system with uniform spatial distribution, it follows in the mean-field limit using the standard Bogoliubov transformations [56–58] that the photon-weighted polariton density of states  $D_P(\omega)$  can be written as (see SI)

$$D_P(\omega) = \sum_{m=0}^{\infty} \left( 1 - \frac{\delta_{0,m}}{2} \right) \frac{q(m, \omega) P_C(\omega)}{\pi v_g(\omega, q) L_C} \theta[\omega_C(\omega) - \frac{m\pi c}{L_C}], \quad (11)$$

where  $\theta(x) = 1$  for  $x \geq 0$  and vanishes elsewhere,  $\omega_C(\omega)$  is the frequency of the photon mode that under strong coupling leads to the formation of a polariton with frequency  $\omega$ ,  $P_C(\omega)$  is the frequency-dependent photon content of polaritons with frequency  $\omega$

$$P_C(\omega) = \frac{(\omega^2 - \omega_M^2 - \Omega_R^2)^2}{(\omega^2 - \omega_M^2 - \Omega_R^2)^2 + \omega_C^2(\omega)\Omega_R^2}, \quad (12)$$

$\omega_M$  is the matter oscillator frequency,  $\Omega_R$  is the collective light-matter interaction strength, and the polariton group velocity ( $v_g$ ) is given by

$$v_g(\omega, q) = \frac{qc^2}{2\omega} \left( 1 \pm \frac{\omega_C^2 - \omega_M^2 + \Omega_R^2}{\sqrt{(\omega_C^2 + \omega_M^2 + \Omega_R^2)^2 - 4\omega_C^2\omega_M^2}} \right), \quad (13)$$

where the positive sign applies when  $\omega$  belongs to an upper polariton branch, i.e.,  $\omega > \omega_C$ , and the negative sign is used if  $\omega < \omega_C$ . In this expression, we have omitted the frequency dependence of  $\omega_C$  for simplicity.

Our model shows singular behavior for  $D_P(\omega)$  as  $\omega \rightarrow \omega_M$ . In this limit, both the photon content  $P_C(\omega)$  and the group velocity  $v_g(\omega, q)$  approach zero, but the ratio  $P_C(\omega)/v_g(\omega, q) \rightarrow \infty$  resulting in  $D_P(\omega)$  diverging to positive infinity. This singularity is due to the formation of the well-known stopgap region[59–62] where  $D_P(\omega) = 0$ . As previous work shows [63], introducing an ultraviolet cutoff and material disorder eliminates the singularity of  $D_P(\omega)$  at  $\omega_M$ . Nevertheless, there remains significant enhancement of  $D_P(\omega)$  in a neighborhood of  $\omega_M$ , which depends in a non-universal way on the type of disorder and coherence loss mechanism. This motivates our decision to use the formally exact expression presented in Eq. 11 and interpret our results as upper bounds on the effect of polaritons on BIRD.

### III Results and Discussion

#### Microcavity-assisted blackbody infrared radiative dissociation

Our analysis of radiative dissociation in weakly coupled microcavities assumes a single diatomic molecule (or a dilute sample at low enough pressure that collisions can be neglected) in a planar microcavity. The tunable electromagnetic environment afforded by the microcavity allows BIRD rates to be either enhanced or suppressed relative to free space, depending on which transitions are significantly affected by the modified photon DOS.

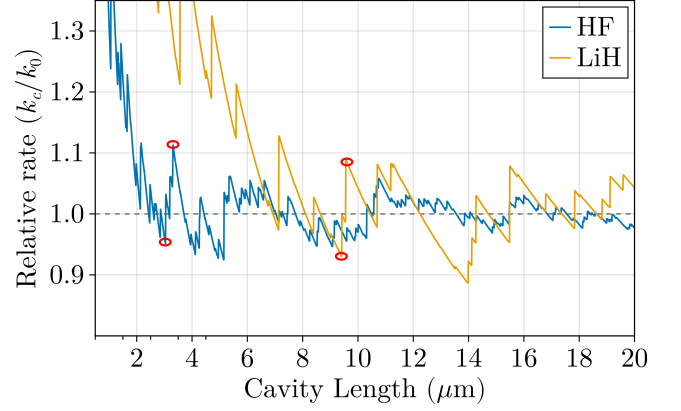


FIG. 2. Ratio of BIRD rate inside a microcavity (weak coupling regime) to the free-space rate as a function of microcavity length for HF and LiH molecules. Red circles highlight specific lengths further discussed in Fig. 3.

In Fig. 2, BIRD rates in the weak coupling regime are shown relative to the free space rate ( $k_0 = 2.70 \times 10^{-6} \text{ s}^{-1}$  for HF at  $T/\omega_e = 0.67$  corresponding to  $T = 4000 \text{ K}$  and  $k_0 = 1.64 \times 10^{-5} \text{ s}^{-1}$  for LiH at  $T/\omega_e = 0.99$  corresponding to  $T = 2000 \text{ K}$ ). For small microcavity lengths, i.e.,  $L_C < 2 \text{ }\mu\text{m}$  for HF and  $L_C < 5 \text{ }\mu\text{m}$  for LiH, a mild but consistent enhancement of BIRD rates is observed. At these lengths, an overall increase in the microcavity electromagnetic DOS over a wide frequency range covering several important transitions is associated with the observed enhancement. The ratios of microcavity BIRD rates to free space BIRD rates quickly approach 1.0 as  $L_C$  increases beyond a few microns. This is expected since the microcavity DOS converges to the free space limit when  $L_C \rightarrow \infty$ .

The complex oscillatory pattern in the BIRD rates relative to free space shown in Fig. 2 arises from the interplay of discrete vibrational transitions enhanced or suppressed depending on  $L_C$ . As we demonstrate below, this complexity is caused by overtones, which play an essential role in our analysis.

We conducted a sensitivity analysis of the dissociation rate to interpret the origin of the oscillatory behavior in Fig. 2 and identify the most consequential radiative transitions involved in the BIRD of HF and LiH. This analysis measures how impactful an enhancement in the photon DOS at a specific transition frequency is to the dissociation process (see Supporting Information for more details). For HF dissociation, changes in the photon density of states corresponding to the frequency of overtone transitions  $i \rightarrow 23$ , with  $i \in \{16, 17, 19\}$  (in the relevant  $1500 - 5000 \text{ cm}^{-1}$  frequency range) are the most consequential for the BIRD rate. Similarly, for LiH, the relevant transitions are  $i \rightarrow 29$ , with  $i \in \{21, 22, 23, 25\}$ . In both cases, the identified overtones take the vibrational mode to the highest energy-bound state (23 for HF and 29 for LiH), from which dissociation rapidly occurs. We emphasize that overtones are crucial because, at high excitation levels, fundamental transitions ( $i \rightarrow i + 1$ ) involve very small energies

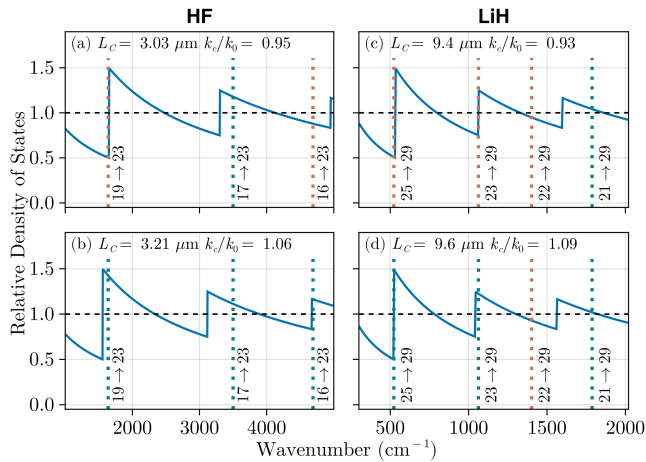


FIG. 3. Microcavity photon DOS normalized to the free space DOS for selected lengths ( $L_C$ ) where BIRD suppression and enhancement were observed for HF (left panels) and LiH (right panels) in Fig. 2. The dotted vertical lines indicate the location of the transition frequencies corresponding to the most relevant overtone transitions, with color coding to distinguish between suppression (red) and enhancement (green). Panel (a) shows that the small HF BIRD suppression observed at  $L_C = 3.03 \mu\text{m}$  is at least in part caused by the reduced relative DOS at the highlighted overtones. Panel (b) shows the mild enhancement of HF BIRD in a microcavity with  $L_C = 3.21 \mu\text{m}$  can be ascribed to the greater microcavity photon DOS at the frequencies of the highlighted overtones. Panels (c) and (d) show the analogous scenario for LiH, where BIRD is observed to be suppressed at  $L_C = 9.4 \mu\text{m}$  but enhanced at  $L_C = 9.6 \mu\text{m}$ , primarily due to the variation of the microcavity photon density of states at the selected  $i \rightarrow 29$  overtone frequencies.

and, therefore, have associated small thermal photon populations and reduced oscillator strengths. See Supporting Information for a brief discussion of results obtained without overtone transitions.

Equipped with the knowledge of the most relevant transitions for the investigated BIRD of HF and LiH via the most energetic bound state, we can readily explain the microscopic origin of the intricate pattern in Fig. 2 by considering how the microcavity DOS changes around the previously mentioned overtones. Fig. 3 presents the ratio of the microcavity DOS to the free space for selected values of  $L_C$  where BIRD suppression or enhancement was verified in Fig. 2 (red circles). Overtone frequencies are highlighted with dotted vertical lines, color-coded by whether they are enhanced (green) or suppressed (red) in the corresponding microcavity. In Fig. 3(a) ( $L_C = 3.03 \mu\text{m}$ ), the most relevant HF overtones are suppressed, and this leads to the observed local minimum in  $k_c/k_0$  in Fig. 2. In contrast, when the microcavity length slightly increases to  $L_C = 3.21 \mu\text{m}$  [Fig. 3(b)] the photon DOS is enhanced at the  $16 \rightarrow 23$  and  $19 \rightarrow 23$  transitions frequencies, and we observe a corresponding leap in the BIRD rate in Fig. 2. Similarly, in Fig. 3(c) ( $L_C = 9.4 \mu\text{m}$ ), all of the relevant LiH overtones but  $21 \rightarrow 29$  are suppressed, leading to a reduced BIRD rate in this microcavity relative to free

space, whereas Fig. 3(d) shows that at  $L_C = 9.6 \mu\text{m}$  most of the relevant LiH overtones are enhanced, thus explaining the sudden increase in BIRD rate at  $L_C = 9.6 \mu\text{m}$  relative to  $L_C = 9.4 \mu\text{m}$ . Introducing a finite linewidth to the considered radiative transitions would smooth out the oscillations observed in Fig. 2 and dampen their amplitude. Consequently, the weakly coupled microcavity effect on BIRD would be significant only at lengths less than a few microns.

Note that suppression effects are generally minor in Fig. 2 because the dissociative process has many pathways. Therefore, blocking or slowing down a particular transition may reduce the dissociation rate, but the effect is almost always negligible as the molecular system explores alternative dissociation pathways. Our analysis of BIRD in weak coupling reveals two main results we expect to hold generically for chemistry in microcavities: (i) overtone transitions are crucial and should not be ignored, and (ii) blocking a single reactive pathway is likely inconsequential.

### Polariton-assisted blackbody infrared radiative dissociation

To analyze polariton-assisted BIRD, we considered a microcavity containing, in addition to the reactive diatomic molecule, a host material strongly coupled with the resonator modes. Fig. 1(d) illustrates this scenario, emphasizing the formation of polariton states, which effectively change the photon frequency-momentum dispersion relation [Fig. 1 (e)] and the electromagnetic DOS. We explore the implications for diatomic BIRD via the most energetic bound state below.

Fig. 4 presents the ratio of polariton-assisted BIRD to the corresponding free space rates ( $k_p/k_0$ ) as a function of the host matter frequency,  $\omega_M$ . These computations were performed with  $\Omega_R = 400 \text{ cm}^{-1}$  and  $200 \text{ cm}^{-1}$  by fixing  $L_C$  at  $3.21$  and  $9.60 \mu\text{m}$  for HF and LiH respectively. As discussed in the previous section, these choices for  $L_C$  enhance the dissociation rate in the weak coupling regime. We observe prominent peaks for HF and LiH where the relative dissociation rate is notably enhanced. Maximal enhancement occurs when the matter frequency ( $\omega_M$ ) is greater than but sufficiently close to a particular diatomic overtone transition frequency we denote by  $\omega_{i \rightarrow j}$ . Here, we focus on the case where  $i = 17$  and  $j = 23$  for HF and  $i = 22$  and  $j = 29$  for LiH. In contrast, the inset of Figs. 4(a) and (c) show that when  $\omega_M$  approaches the diatomic transition from the left, the dissociation reaction is suppressed. This suppression occurs because as  $\omega_M - \omega_{i \rightarrow j} \rightarrow 0^-$ , the overtone transition falls into the stopgap region of the polaritonic dispersion, where the electromagnetic DOS is zero (Fig. 1e). However, the BIRD suppression is relatively small since, as discussed earlier, the reaction may still proceed through alternative pathways.

The effect of the collective coupling strength ( $\Omega_R$ ) on the relative polariton-assisted BIRD rates is examined in Fig. 4(b) and (d). When  $\omega_M - \omega_{i \rightarrow j}$  is around  $0.01\text{-}1 \text{ cm}^{-1}$ , increasing  $\Omega_R$  results in greater polariton-assisted BIRD rates. However, as  $\omega_M$  becomes arbitrarily close to  $\omega_{i \rightarrow j}$ , the polaritonic enhancement of BIRD saturates around 20 and 50 for LiH and HF, respectively. This plateau appears to be insensitive to the magnitude of the Rabi splitting. It can be explained by the sin-

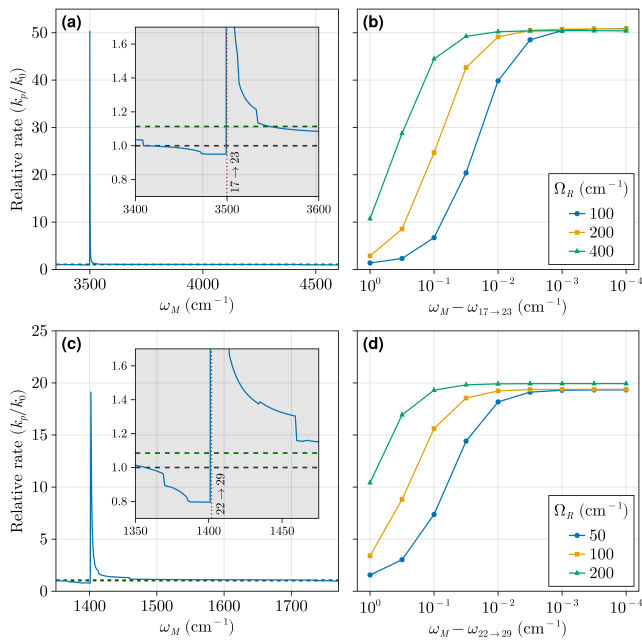


FIG. 4. Ratio of polariton-assisted BIRD rates to free space BIRD rates. In the polaritonic case, the diatomic molecule is embedded in a strongly coupled microcavity with variable host material with frequency  $\omega_M$ . The top panels, (a) and (b), correspond to HF, and the bottom panels, (c) and (d), show results for LiH. In (a) and (c), the collective light-matter interaction strength,  $\Omega_R$ , is fixed at 400 and 200  $\text{cm}^{-1}$ , respectively. The horizontal dashed gray and green lines indicate where the dissociation rates equal  $k_0$  and  $k_c$ , respectively. The insets in (a) and (c) show zoomed-in views around the overtones  $17 \rightarrow 23$  for HF and  $22 \rightarrow 29$  for LiH. In (b) and (d), relative BIRD rates are shown for different Rabi frequencies ( $\Omega_R$ ), depicting the dependency on the detuning between the host molecule and the diatomic transition energies.

gularity in the photon-weighted polariton DOS, which arises as  $\omega \rightarrow \omega_M$  and is illustrated in Fig. 5.

In Fig. 5, the photon-weighted polariton density of states  $D_P(\omega)$  is shown for selected values of  $\Omega_R$  at  $L_C = 9.6 \mu\text{m}$  and  $\omega_M = v_{22 \rightarrow 29}(\text{LiH}) = 1401 \text{ cm}^{-1}$ . The case where  $\Omega_R = 0$  represents the weak coupling limit and is included here to directly compare  $D_P(\omega)$  with  $D_C(\omega)$ . It can be seen from Fig. 5 that the photon-weighted polariton DOS is only fundamentally different from the bare microcavity DOS in a neighborhood of  $\omega_M$  that also contains the stopgap. Most remaining features, e.g., the oscillations in  $D_P(\omega)$  with  $\omega$ , are also observed in weak coupling and can be understood from Eq. 8. The various curves in Fig. 5 illustrate how the width of the stopgap region and the electromagnetic mode frequencies with significantly enhanced  $D_P(\omega)$  expand as  $\Omega_R$  increases. As a result, strong coupling can induce changes in the rates of multiple vibrational transitions depending on the Rabi splitting.

The singularity in the photon-weighted polariton DOS enables a particular radiative overtone transition to become arbitrarily faster than the corresponding free space rate. However, our results demonstrate that this singularity does not

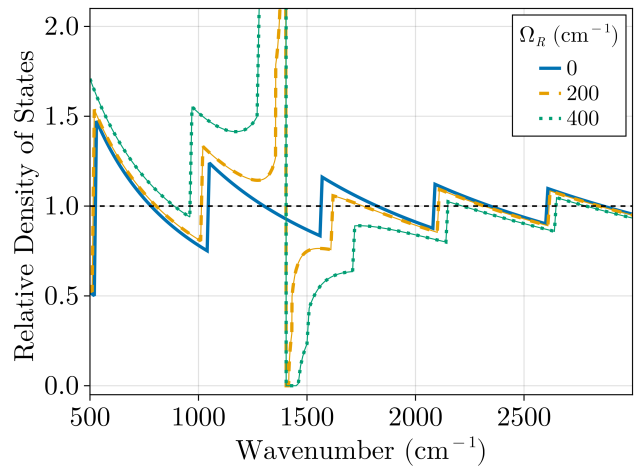


FIG. 5. Photon-weighted polariton density of states  $D_P(\omega)$ , normalized to the free space DOS, for a microcavity with length  $L_C = 9.6 \mu\text{m}$  strongly coupled to a material with a bright transition at frequency  $\omega_M = 1401 \text{ cm}^{-1}$ . The curves show the effect of different Rabi splitting values ( $\Omega_R$ ) on the photon-weighted polariton DOS, which is relevant for radiative processes mediated by polaritonic systems. As  $\Omega_R$  increases, the frequency range below  $\omega_M$ , where the photon-weighted polariton DOS significantly exceeds that of free space, widens. This trend explains the impact of the collective light-matter interaction strength on the observed polariton-assisted bond infrared dissociation (BIRD) enhancement shown in Fig. 4.

lead to arbitrarily fast reaction rates since the complex multi-step reactive process ensures that other transitions quickly become rate-limiting. Therefore, the BIRD rates reported as  $\omega_M \rightarrow \omega_{i \rightarrow j}$  provide a *finite* upper bound for polariton-enhanced BIRD rates in the lossless limit discussed here. In experiments, imperfections in the electromagnetic device and the strongly coupled material smooth out the photon-weighted DOS near the stopgap. Nonetheless, previously reported simulations show the enhancement of  $D_P(\omega)$  persists around  $\omega_M$  in the presence of an ultraviolet cutoff and material disorder [63]. The introduction of a UV cutoff, loss, and dephasing pathways for the material system will lead to reduced BIRD enhancements relative to those in Fig. 4 depending in a non-universal fashion on  $\Omega_R$  and parameters characterizing the quality of the strongly coupled subsystems (e.g., microcavity quality factor, matter homogeneous linewidth, etc).

Including a finite linewidth for the diatomic vibrational transitions relaxes the strict resonance requirement discussed above ( $\omega_M \rightarrow \omega_{i \rightarrow j}$ ), and the overall enhancement will depend on the spectral overlap between  $\omega_{i \rightarrow j}$  and  $D_P(\omega)$ . Since the molecular linewidth and cavity imperfections are expected to be limiting factors, it is clear that our reported results represent theoretical upper bounds for polariton-assisted BIRD rates for the reaction mechanism investigated here.

Before ending, we emphasize our observation of the same qualitative behavior for polariton-mediated BIRD in LiH and HF. Since these chemical species have significantly different energetics, we anticipate the main trends reported in this work also apply to other diatomic and polyatomic molecules, par-

ticularly in cases where dissociation occurs through a specific doorway state.

#### IV Conclusions

This work presented a detailed analysis of BIRD in infrared microcavities. Our analysis revealed mechanisms for controlling dissociation phenomena in microcavities, particularly by manipulating the electromagnetic density of states (DOS) in weak and strong light-matter coupling regimes. Overtones play a critical role in the dissociation process under both weak and strong coupling cases, as the corresponding transitions act as rate-limiting steps for the dissociative process occurring via the highest energy-bound state. The radiative dissociation rate changes induced by a microcavity are essentially tied to how the photonic density of states is modified around specific overtone transitions driving the system into the dissociating (doorway) state.

We reported microcavity-assisted dissociation rate enhancements of  $O(1)$  in the weak coupling regime. In microcavities where  $L_C \leq 5 \mu\text{m}$ , the photon DOS is greater than in free space for most relevant diatomic transitions, leading to a mild increase in dissociation rates. As  $L_C$  increases beyond a few microns, a complex pattern emerges from the interplay between enhanced and suppressed vibrational transitions, which can be rationalized by analyzing a few important overtones. Further increases in  $L_C$  causes the BIRD rates to approach the free-space limit.

In the strong coupling regime, where polaritons mediate BIRD, we reported  $O(10)$  enhancements when the host matter frequency is resonant with rate-limiting overtones of the dissociative process. This enhancement is due to the emer-

gence of a singularity in the photon-weighted polariton DOS, which massively increases transition rates between levels with energy differences that approach the low-energy boundary of the polariton stopgap from below. The singularity is attributed to the lack of a high-energy cutoff for the electromagnetic field and the lossless character of the strongly coupled system. Nevertheless, while the singular behavior of the photon-weighted polariton DOS is absent from experiments, we have argued its effects are expected to persist to an extent that depends on  $\Omega_R$  and parameters controlling losses and disorder. Ultimately, the BIRD enhancement factors reported here provide upper bounds for polariton-induced diatomic thermal radiative dissociation changes via the most energetic bound state.

Our work focused on how optical microcavities can modify BIRD reactions of diatomic molecules via a particular mechanism. Despite focusing on these specific systems, the main qualitative conclusions we drew about BIRD in weak and strong coupling apply broadly. We expect the analysis introduced here will be useful in understanding and controlling generic polyatomic thermal radiative-induced dissociation processes in microcavities.

**Acknowledgments.** This work was supported by the donors of ACS Petroleum Research Fund under Doctoral New Investigator Grant 66399-DNI6. R.F.R. served as Principal Investigator on ACS PRF-66399-DNI6 that provided support for E. S. R.F.R. also acknowledges support from NSF CAREER award Grant No. CHE-2340746, and startup funds provided by Emory University.

**Author Contributions.** G. J. R. A. and E. S. contributed equally to this work.

- 
- [1] A. Thomas, J. George, A. Shalabney, M. Dryzhakov, S. J. Varma, J. Moran, T. Chervy, X. Zhong, E. Devaux, C. Genet, J. A. Hutchison, and T. W. Ebbesen, Ground-State Chemical Reactivity under Vibrational Coupling to the Vacuum Electromagnetic Field, *Angewandte Chemie International Edition* **55**, 11462 (2016).
- [2] A. Thomas, L. Lethuillier-Karl, K. Nagarajan, R. M. A. Vergauwe, J. George, T. Chervy, A. Shalabney, E. Devaux, C. Genet, J. Moran, and T. W. Ebbesen, Tilting a ground-state reactivity landscape by vibrational strong coupling, *Science* **363**, 615 (2019).
- [3] K. Hirai, R. Takeda, J. A. Hutchison, and H. Uji-i, Modulation of prins cyclization by vibrational strong coupling, *Angewandte Chemie* **132**, 5370 (2020).
- [4] W. Ahn, J. F. Triana, F. Recabal, F. Herrera, and B. S. Simpkins, Modification of ground-state chemical reactivity via light-matter coherence in infrared cavities, *Science* **380**, 1165 (2023).
- [5] A. V. Kavokin, J. J. Baumberg, G. Malpuech, and F. P. Laussy, *Microcavities*, Vol. 21 (Oxford University Press, 2017).
- [6] K. Nagarajan, A. Thomas, and T. W. Ebbesen, Chemistry under vibrational strong coupling, *Journal of the American Chemical Society* **143**, 16877 (2021).
- [7] E. Vinogradov, Vibrational polaritons in semiconductor films on metal surfaces, *Physics Reports* **217**, 159 (1992).
- [8] A. Shalabney, J. George, J. Hutchison, G. Pupillo, C. Genet, and T. W. Ebbesen, Coherent coupling of molecular resonators with a microcavity mode, *Nature Communications* **6**, 10.1038/ncomms6981 (2015).
- [9] B. S. Simpkins, K. P. Fears, W. J. Dressick, B. T. Spann, A. D. Dunkelberger, and J. C. Owrutsky, Spanning Strong to Weak Normal Mode Coupling between Vibrational and Fabry-Pérot Cavity Modes through Tuning of Vibrational Absorption Strength, *ACS Photonics* **2**, 1460 (2015).
- [10] J. Galego, C. Climent, F. J. Garcia-Vidal, and J. Feist, Cavity casimir-polder forces and their effects in ground-state chemical reactivity, *Physical Review X* **9**, 021057 (2019).
- [11] J. A. Campos-Gonzalez-Angulo, R. F. Ribeiro, and J. Yuen-Zhou, Resonant catalysis of thermally activated chemical reactions with vibrational polaritons, *Nature communications* **10**, 4685 (2019).
- [12] V. P. Zhdanov, Vacuum field in a cavity, light-mediated vibrational coupling, and chemical reactivity, *Chemical Physics* **535**, 110767 (2020).
- [13] D. S. Wang, J. Flick, and S. F. Yelin, Chemical reactivity under collective vibrational strong coupling, *The Journal of Chemical*

- Physics **157**, 224304 (2022).
- [14] L. P. Lindoy, A. Mandal, and D. R. Reichman, Resonant cavity modification of ground-state chemical kinetics, *The Journal of Physical Chemistry Letters* **13**, 6580 (2022).
- [15] C. Schäfer, J. Flick, E. Ronca, P. Narang, and A. Rubio, Shining light on the microscopic resonant mechanism responsible for cavity-mediated chemical reactivity, *Nature Communications* **13**, 7817 (2022).
- [16] J. Sun and O. Vendrell, Suppression and enhancement of thermal chemical rates in a cavity, *The Journal of Physical Chemistry Letters* **13**, 4441 (2022).
- [17] S. Montillo Vega, W. Ying, and P. Huo, Theory of resonance suppression in vibrational polariton chemistry, *ChemRxiv* 10.26434/chemrxiv-2024-m7t4c (2024).
- [18] Y. Lai, W. Ying, and P. Huo, Non-equilibrium rate theory for polariton relaxation dynamics, *The Journal of Chemical Physics* **161**, 104109 (2024).
- [19] N. Moiseyev, Conditions for enhancement of chemical reactions in gas phase inside a dark cavity (2024), arXiv:2405.11387 [quant-ph].
- [20] B. S. Simpkins, A. D. Dunkelberger, and J. C. Owrutsky, Mode-specific chemistry through vibrational strong coupling (or a wish come true), *The Journal of Physical Chemistry C* **125**, 19081 (2021).
- [21] J. A. Campos-Gonzalez-Angulo, Y. R. Poh, M. Du, and J. Yuen-Zhou, Swinging between shine and shadow: Theoretical advances on thermally activated vibropolaritonic chemistry, *The Journal of Chemical Physics* **158** (2023).
- [22] R. C. Dunbar, Bird (blackbody infrared radiative dissociation): evolution, principles, and applications, *Mass spectrometry reviews* **23**, 127 (2004).
- [23] J. Perrin, *Les atomes*. 1913, English edition: *Atoms*, tr. D. Hamrick.(Constable, 1923) (1970).
- [24] F. A. Lindemann, S. Arrhenius, I. Langmuir, N. Dhar, J. Perrin, and W. M. Lewis, Discussion on “the radiation theory of chemical action”, *Transactions of the Faraday Society* **17**, 598 (1922).
- [25] F. Daniels, The radiation hypothesis of chemical reaction., *Chemical Reviews* **5**, 39 (1928).
- [26] M. C. King and K. J. Laidler, Chemical kinetics and the radiation hypothesis, *Archive for History of Exact Sciences* , 45 (1984).
- [27] D. Thoelmann, D. S. Tonner, and T. B. McMahon, Spontaneous unimolecular dissociation of small cluster ions,  $(\text{H}_3\text{O}^+)_n$  and  $\text{Cl}(\text{H}_2\text{O})_n$  ( $n=2-4$ ), under fourier transform ion cyclotron resonance conditions, *The Journal of Physical Chemistry* **98**, 2002 (1994).
- [28] R. C. Dunbar, T. B. McMahon, D. Thoelmann, D. S. Tonner, D. R. Salahub, and D. Wei, Zero-pressure thermal-radiation-induced dissociation of gas-phase cluster ions: Comparison of theory and experiment for  $(\text{H}_2\text{O})_2\text{Cl}^-$  and  $(\text{H}_2\text{O})_3\text{Cl}^-$ , *Journal of the American Chemical Society* **117**, 12819 (1995).
- [29] P. D. Schnier, W. D. Price, R. A. Jockusch, and E. R. Williams, Blackbody infrared radiative dissociation of bradykinin and its analogues: Energetics, dynamics, and evidence for salt-bridge structures in the gas phase, *Journal of the American Chemical Society* **118**, 7178 (1996).
- [30] R. C. Dunbar and T. B. McMahon, Activation of unimolecular reactions by ambient blackbody radiation, *Science* **279**, 194 (1998).
- [31] S. M. Stevens, R. C. Dunbar, W. D. Price, M. Sena, C. H. Watson, L. S. Nichols, J. M. Riveros, D. E. Richardson, and J. R. Eyler, Blackbody infrared radiative dissociation of partially solvated tris(2,2'-bipyridine)ruthenium(II) complex ions, *The Journal of Physical Chemistry A* **106**, 9686 (2002).
- [32] W. G. Valance and E. W. Schlag, Theoretical rate constant for thermal unimolecular reactions in a multilevel system, *The Journal of Chemical Physics* **45**, 216 (1966).
- [33] R. G. Gilbert and S. C. Smith, *Theory of Unimolecular and Recombination Reactions* (Blackwell Scientific Publications, Oxford, UK, 1990).
- [34] E. Fermi, Quantum theory of radiation, *Reviews of Modern Physics* **4**, 87 (1932).
- [35] J. J. Sakurai and J. Napolitano, *Modern Quantum Mechanics*, 2nd ed. (Cambridge University Press, Cambridge, 2017).
- [36] A. Einstein, Zur quantentheorie der strahlung, *Phys Zeit* **18**, 121 (1917).
- [37] C. Cohen-Tannoudji, B. Diu, and F. Laloë, *Quantum Mechanics, Volume 1: Basic Concepts, Tools, and Applications* (John Wiley & Sons, 2019).
- [38] S. N. Bose, Plancks gesetz und lichtquantenhypothese, *Zeitschrift für Physik* **26**, 178 (1924).
- [39] P. M. Morse, Diatomic molecules according to the wave mechanics. ii. vibrational levels, *Physical Review* **34**, 57 (1929).
- [40] D. M. Bishop, Vibrational transition moments in diatomic molecules, *Reviews of Modern Physics* **62**, 343 (1990).
- [41] M. Kaluža, J. T. Muckerman, P. Gross, and H. Rabitz, Optimally controlled five-laser infrared multiphoton dissociation of HF, *The Journal of Chemical Physics* **100**, 4211 (1994).
- [42] J. Stine and D. Noid, Classical treatment of the dissociation of hydrogen fluoride with one and two infrared lasers, *Opt. Commun* **31**, 161–164 (1979).
- [43] A. Guldberg and G. D. Billing, Laser-induced dissociation of hydrogen fluoride, *Chem. Phys. Lett* **186**, 229–237 (1991).
- [44] P. Gross, D. Neuhauser, and H. Rabitz, Teaching lasers to control molecules in the presence of laboratory field uncertainty and measurement imprecision, *J. Chem. Phys.* **98**, 4557–4566 (1993).
- [45] K. K. Irikura, Experimental vibrational zero-point energies: Diatomic molecules, *JPCRD* **36**, 389–397 (2007).
- [46] W. D. Price, P. D. Schnier, and E. R. Williams, Binding energies of the proton-bound amino acid dimers gly.gly, ala.ala, gly.ala, and lys.lys measured by blackbody infrared radiative dissociation, *J Phys Chem B* **101**, 664 (1997).
- [47] H. Zoubi and G. La Rocca, Microscopic theory of anisotropic organic cavity exciton polaritons, *Physical Review B* **71**, 235316 (2005).
- [48] J. D. Jackson, *Classical electrodynamics* (John Wiley & Sons, 2021).
- [49] W. L. Barnes, S. A. R. Horsley, and W. L. Vos, Classical antennas, quantum emitters, and densities of optical states, *J. Opt.* **22**, 073501 (2020).
- [50] E. A. Power and S. Zienau, Coulomb gauge in non-relativistic quantum electrodynamics and the shape of spectral lines, *Philosophical Transactions of the Royal Society A: Mathematical, Physical and Engineering Sciences* **251**, 427 (1959).
- [51] R. G. Woolley, Quantum electrodynamics and molecular physics, *Proceedings of the Royal Society of London. Series A, Mathematical and Physical Sciences* **321**, 557 (1971).
- [52] E. A. Power and T. Thirunamachandran, Quantum electrodynamics in a cavity, *Physical Review A* **25**, 2473 (1982).
- [53] D. Craig and T. Thirunamachandran, *Molecular Quantum Electrodynamics: An Introduction to Radiation-molecule Interactions*, Dover Books on Chemistry Series (Dover Publications, 1998).
- [54] Y. Ashida, A. İmamoğlu, J. Faist, D. Jaksch, A. Cavigliari, and E. Demler, Quantum electrodynamic control of matter: Cavity-enhanced ferroelectric phase transition, *Physical Review X* **10**,

- 041027 (2020).
- [55] J. B. Curtis, M. H. Michael, and E. Demler, Local fluctuations in cavity control of ferroelectricity, *Physical Review Research* **5**, 043118 (2023).
- [56] N. N. Bogoliubov, On a new method in the theory of superconductivity, *Il Nuovo Cimento* **7**, 794 (1958).
- [57] J. J. Hopfield, Theory of the Contribution of Excitons to the Complex Dielectric Constant of Crystals, *Physical Review* **112**, 1555 (1958).
- [58] V. M. Agranovich and V. L. Ginzburg, *Crystal Optics with Spatial Dispersion, and Excitons* (Springer-Verlag, Berlin, 1984).
- [59] M. Litinskaya and V. Agranovich, In-gap polaritons in uniformly filled microcavities, *Journal of Physics: Condensed Matter* **21**, 415301 (2009).
- [60] K. C. Huang, P. Bienstman, J. D. Joannopoulos, K. A. Nelson, and S. Fan, Theory of thermal emission from a finite photonic crystal slab, *Physical Review B* **68**, 075209 (2003).
- [61] J. Gómez Rivas, M. Kuttge, P. Haring Bolivar, H. Kurz, and J. A. Sánchez-Gil, Propagation of surface plasmon polaritons on semiconductor gratings, *Physical Review Letters* **93**, 256804 (2004).
- [62] Y. Todorov and C. Sirtori, Intersubband polaritons in the electrical dipole gauge, *Physical Review B* **85**, 045304 (2012).
- [63] A. M. Satanin, Y. S. Joe, C. S. Kim, and M. I. Vasilevskiy, Localization of phonon polaritons in disordered polar media, *Physical Review E* **72**, 066618 (2005).

# Supplementary Material: Polaritonic Control of Blackbody Infrared Radiative Dissociation

Enes Suyabatmaz,<sup>1</sup> Gustavo J. R. Aroeira,<sup>2</sup> and Raphael F. Ribeiro<sup>2,\*</sup>

<sup>1</sup>Department of Physics, Emory University, Atlanta, GA, 30322

<sup>2</sup>Department of Chemistry, Emory University, Atlanta, GA, 30322

(Dated: November 1, 2024)

## S1. Model parameters for HF and LiH

We use a Morse potential to describe the potential energy of the examined diatomic molecules,

$$V(r) = D_e \left(1 - e^{-\alpha(r-r_e)}\right)^2, \quad (\text{S1})$$

where

$$\alpha = \sqrt{\frac{k_e}{2D_e}}, \quad (\text{S2})$$

$$k_e = m_r(2\pi c\nu_e)^2, \quad (\text{S3})$$

with  $c$  being the speed of light in the vacuum,  $m_r$  the reduced mass and  $\nu_e$  the harmonic frequency of the system. The energy levels are calculated as

$$E(n)/hc = \nu_e \left(n + \frac{1}{2}\right) - \nu_e \chi_e \left(n + \frac{1}{2}\right)^2, \quad (\text{S4})$$

where  $n$  is the vibrational quantum number,  $h$  is Planck's constant and  $\chi_e$  is the anharmonicity constant. The number of bound states is given by

$$n_{\max} = \left\lfloor \frac{\sqrt{2m_r D_e}}{\hbar\alpha} - \frac{1}{2} \right\rfloor. \quad (\text{S5})$$

For the HF molecule, we obtained all Morse parameters from previous work on laser-induced dissociation [1–4]. For LiH, harmonic and anharmonic frequencies were obtained from experimental data[5], and the dissociation energy was extrapolated from these parameters using the following relationship valid for a Morse potential:

$$D_e = \frac{hc\nu_e^2}{4(\nu_e\chi_e)}. \quad (\text{S6})$$

The dissociation energy ( $D_e$ ) obtained using this method (2.641 eV) deviates slightly from reported experimental[5–7] and other *ab initio* computations[8–10] (approximately 2.515 eV). This discrepancy arises because the electronic ground-state LiH potential energy curve deviates from the Morse potential assumed for simplicity in Eq. S6. However, we emphasize that the parameters used for both HF and LiH are representative of these species, and a more precise description would not change the conclusions of this work in any significant way.

The equilibrium bond length ( $r_e$ ) for LiH was computed with CCSD(T)/aug-cc-pVTZ. All used Morse potential parameters are collected in Table 1 in the main manuscript. Morse potentials corresponding to the given parameters are shown in Fig. S1

\* raphael.ribeiro@emory.edu

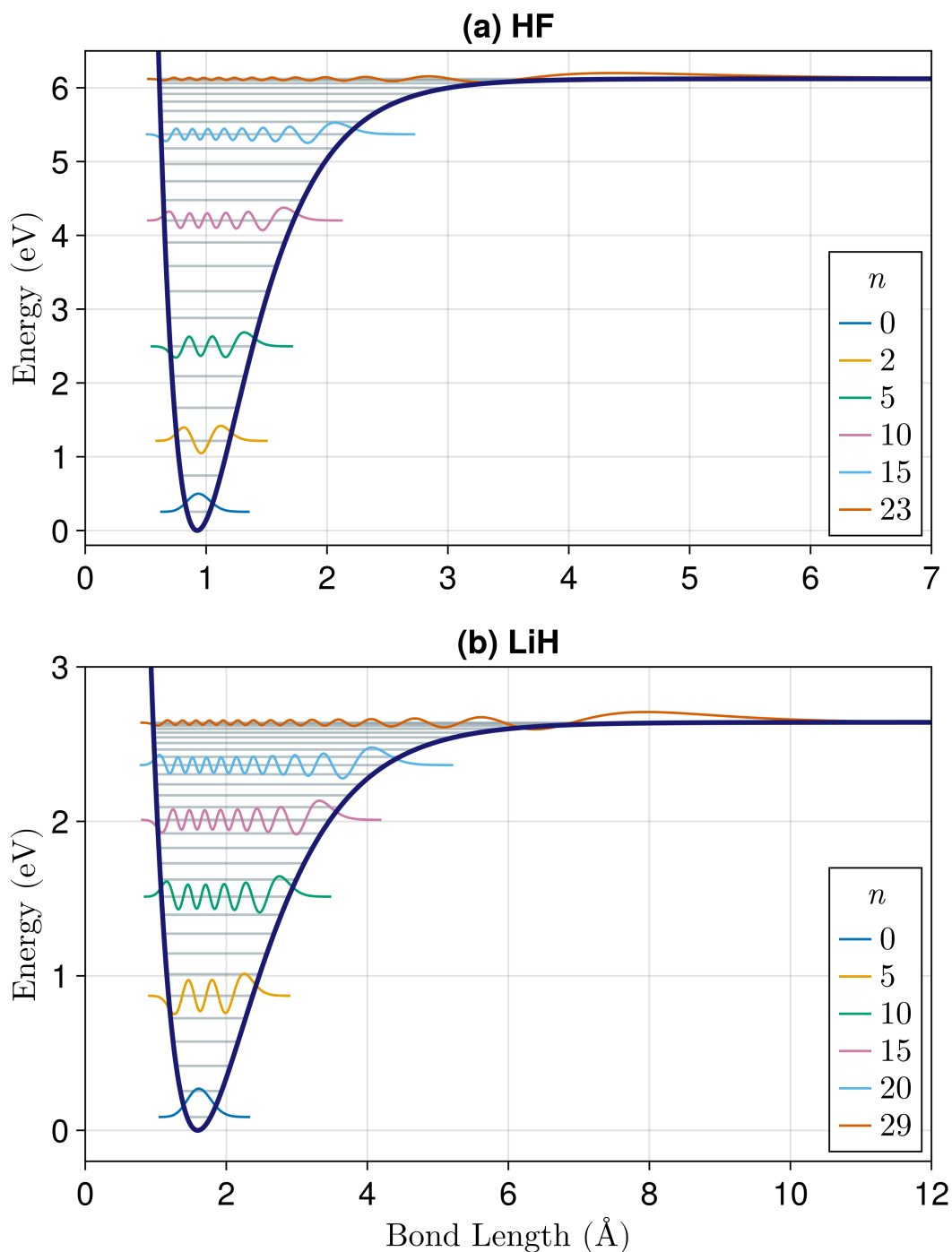


FIG. S1. Morse potential and energy levels (shown as horizontal lines) used in this work for (a) HF and (b) LiH. Selected vibrational wave functions are also shown. They are shifted according to their corresponding energy for better visualization.

along with selected wave functions. The wave functions are computed as described by Dahl and Springborg[11]. In Fig. S1, their extension is truncated when their amplitudes squared are below  $1 \times 10^{-8}$ , giving us an idea of their spatial extent. It can be seen, for example, that in both cases, the final bound state ( $n = 23$  and  $29$  for HF and LiH, respectively) spans a bigger domain than lower energy states. Consequently, they require a large integration grid to compute dipole transition matrix elements, which we will discuss next.

Electrical dipole transition matrix elements  $\mu_{ij}$  can be computed from the vibrational wave functions as

$$\mu_{ij} = \int_{-\infty}^{+\infty} \psi_i^*(r)\mu(r)\psi_j(r)dr, \quad (\text{S7})$$

where  $\psi_k(r)$  represents the  $k$ -th vibrational state and  $\mu(r)$  describes the electronic dipole moment change dependence on  $r$ . For HF, we use the same dipole function employed in previous work[1–4]:

$$\mu(r) = \mu_0 r e^{-\zeta r^4}, \quad (\text{S8})$$

with the parameters shown in Table S1.

TABLE S1. Dipole function parameters for HF.

Constant	
$\mu_0$ ( $e$ )	0.4541416929
$\zeta$ ( $\text{\AA}^{-4}$ )	0.081616

In the case of LiH, we computed electronic ground-state dipole moments for a range of bond lengths with CCSD/aug-cc-pVTZ using Psi4 1.9.1.[12] The calculated values are shown in Table S2. We used a smooth interpolation over these points to make it suitable for numerical integration.

Fig. S2 shows the dipole functions for LiH and HF. Calculating dipoles for small bond lengths becomes increasingly difficult due to convergence issues. This region of configuration space is irrelevant for the computation of transition dipole matrix elements since the vibrational wave functions decay exponentially at small  $r$  (see Fig. S1). Hence, we enforce  $\mu \rightarrow 0$  in the interpolation as  $r \rightarrow 0$ . This has no impact on the computed transition dipole matrix elements. Eq. S7 is evaluated numerically with integration domain spanning  $r_{\min} = 0.0 \text{ \AA}$  to  $r_{\max} = 25 \text{ \AA}$  with a grid spacing of  $0.01 \text{ \AA}$ .

TABLE S2. Computed dipole values for LiH at the CCSD/aug-cc-pVTZ level of theory

Bond length (Å)	Dipole moment ( $e \cdot \text{Å}$ )	Bond length (Å)	Dipole moment ( $e \cdot \text{Å}$ )
0.8	1.001784	3.8	0.906715
0.9	1.005755	3.9	0.794486
1.0	1.020283	4.0	0.688254
1.1	1.042796	4.1	0.590553
1.2	1.071374	4.2	0.502836
1.3	1.104625	4.3	0.425616
1.4	1.141516	4.4	0.358684
1.5	1.181232	4.5	0.30136
1.6	1.22307	4.6	0.252706
1.7	1.266371	4.7	0.211681
1.8	1.31048	4.8	0.177251
1.9	1.354716	4.9	0.148449
2.0	1.398346	5.0	0.124402
2.1	1.440576	5.1	0.104353
2.2	1.480534	5.2	0.087644
2.3	1.517256	5.3	0.073719
2.4	1.549676	5.4	0.062111
2.5	1.576608	5.5	0.052427
2.6	1.596731	5.6	0.044341
2.7	1.608595	5.7	0.037582
2.8	1.610629	5.8	0.031925
2.9	1.601195	5.9	0.027184
3.0	1.578687	6.0	0.023205
3.1	1.541688	6.1	0.019858
3.2	1.489204	6.2	0.017039
3.3	1.420938	6.3	0.014659
3.4	1.337587	6.4	0.012647
3.5	1.241024	6.5	0.010942
3.6	1.134302	6.6	0.009493
3.7	1.021397		

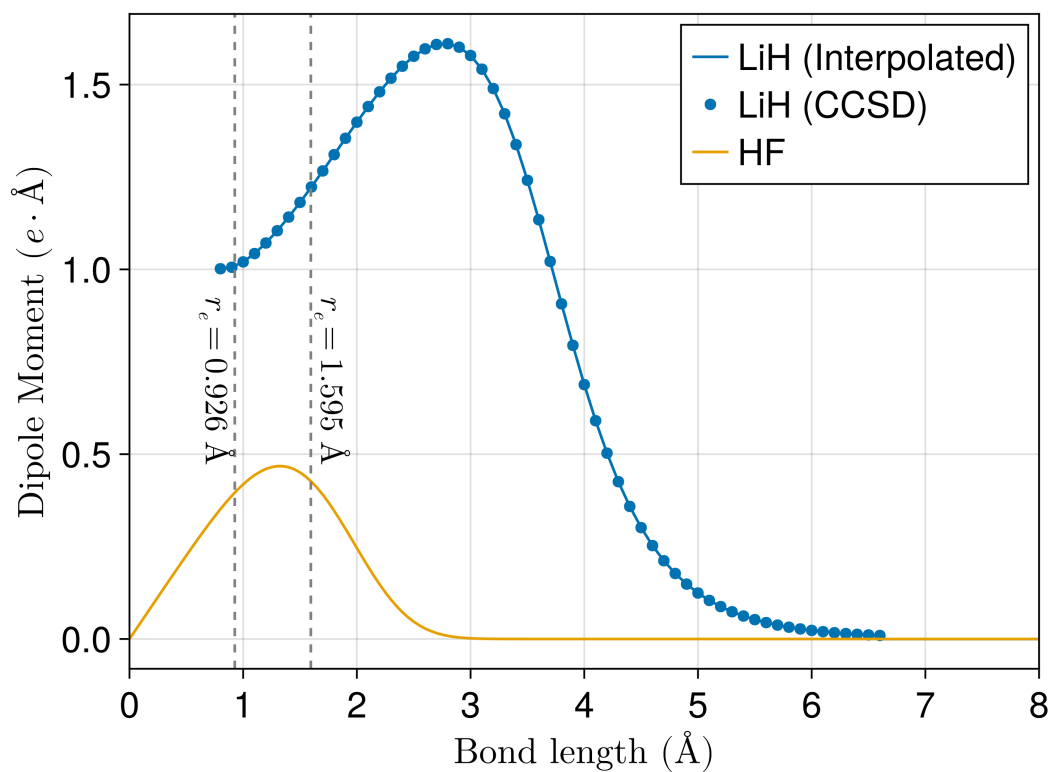


FIG. S2. Dipole functions for HF and LiH. We use a model function described in Eq. S8 for HF. For LiH, we calculated dipole moments at the CCSD level of theory with the aug-cc-pVTZ basis set (blue circles) and used interpolation to obtain a smooth function. Dashed vertical lines indicate the equilibrium radius for HF (0.926 Å) and LiH (1.595 Å).

## S2. Rate Constant from Master Equation

The dynamics of the reactive molecule is modeled with a Markov Master equation routinely employed in studies of blackbody infrared radiative molecules in free space [13]. In this formalism, the time evolution of the vibrational population vector  $[\mathbf{N}] = [N_1, N_2, \dots, N_n]$  is described by the equation

$$\frac{d[\mathbf{N}]}{dt} = -\mathbf{J} \cdot [\mathbf{N}], \quad (\text{S9})$$

where  $N_\nu$  is the population of state  $\nu$ ,  $n = n_{\max}$  (Eq. S5), and  $\mathbf{J}$  is the transition matrix

$$\mathbf{J} = \begin{pmatrix} (k_{12} + \dots + k_{1n}) & -k_{21} & \dots & -k_{n1} \\ -k_{12} & (k_{21} + \dots + k_{2n}) & \dots & -k_{n2} \\ \vdots & \vdots & \ddots & \vdots \\ -k_{1n} & -k_{2n} & \dots & k_{\text{loss}} \end{pmatrix}. \quad (\text{S10})$$

Each matrix element  $J_{ij}$  with  $i \neq j$  corresponds to the transition rate  $k_{ij}$  from state  $i$  to state  $j$ . Diagonal elements  $J_{ii}$  represent the total outgoing rate from state  $i$ . This includes all transitions from state  $i$  to every other state  $j$ . The diagonal elements are always positive. The last row of  $\mathbf{J}$  includes  $k_{\text{loss}}$ , which represents the irreversible loss of population due to the dissociation in the highest energy bound level.

The eigenvalues of the transition matrix  $J$  are guaranteed to be positive[14], and the smallest eigenvalue  $\lambda_1$  of  $\mathbf{J}$  is the rate constant of the unimolecular reaction. This is because, in the long-time limit, the system relaxes to the slowest decaying mode, i.e., the smallest eigenvalue of the transition matrix.

To show that the smallest eigenvalue gives the reaction rate constant, we note that the solution to Eq. S9 can be expressed as [15]:

$$[\mathbf{N}(t)] = \sum_{i=1}^n c_i e^{-\lambda_i t} [\mathbf{v}_i], \quad (\text{S11})$$

where  $\lambda_i$  are the eigenvalues of  $\mathbf{J}$ , and  $[\mathbf{v}_i]$  are the corresponding eigenvectors. Let the eigenvalues be ordered as  $\lambda_1 < \lambda_2 < \dots < \lambda_n$ . As  $t \rightarrow \infty$ , the term with the smallest eigenvalue  $\lambda_1$  dominates the time evolution and all of the remaining  $e^{-\lambda_2 t}, \dots, e^{-\lambda_n t}$  approach zero rapidly because their corresponding  $\lambda_i$  values are larger than  $\lambda_1$ . The term  $e^{-\lambda_1 t}$  gives the slowest decay, since  $\lambda_1$  is the smallest. This means that the slowest decaying term effectively dominates the sum after a sufficiently long induction time  $t \gg 1/\lambda_2$  leading to

$$[\mathbf{N}(t)] \sim c_1 e^{-\lambda_1 t} [\mathbf{v}_1], \quad t \gg 1/\lambda_2 \quad (\text{S12})$$

where  $c_1$  is a constant determined by the initial conditions. This shows that the population at any energy level decays at the same rate  $\lambda_1$  and thus  $\lambda_1$  is the unimolecular reaction rate[16].

### S3. Free space thermal radiation

The Hamiltonian for the free photon field, which describes the energy of a system of non-interacting photons, is given by:

$$H_0 = \sum_{\mathbf{k}, \lambda} \hbar \omega_{\mathbf{k}} a_{\mathbf{k}, \lambda}^{\dagger} a_{\mathbf{k}, \lambda}, \quad (\text{S13})$$

where  $\mathbf{k}$  is the wave vector,  $\lambda = 1, 2$  is the polarization,  $\omega_{\mathbf{k}}$  is the angular frequency of the mode with wave vector  $\mathbf{k}$ , and  $a_{\mathbf{k}, \lambda}^{\dagger}$  and  $a_{\mathbf{k}, \lambda}$  are the creation and annihilation operators for the photon in that mode.

The free electromagnetic field partition function  $Z(\beta) = \text{tr}(e^{-H/k_B T})$  allows us to compute all thermodynamic quantities of the bare field. The total radiation thermal energy at inverse temperature  $\beta = 1/k_B T$  is given by

$$E(T) = -\frac{\partial \log Z(\beta)}{\partial \beta} = \sum_{\lambda} \frac{\hbar \omega_{\mathbf{k}}}{e^{\hbar \omega_{\mathbf{k}}/k_B T} - 1}, \quad (\text{S14})$$

and the mean photon number for a mode with frequency  $\omega$  is given by

$$n(\omega, T) = \frac{1}{e^{\frac{\hbar \omega_{\mathbf{k}}}{k_B T}} - 1}. \quad (\text{S15})$$

The density of photon states  $D_0(\omega)$  corresponds to the number of available electromagnetic modes per unit frequency per unit volume at a frequency  $\omega$ . For simplicity, we consider free space to be a three-dimensional periodic box with lengths  $L_x = L_y = L_z = L$ . The free space DOS is given by[17]:

$$D_0(\omega) = \frac{1}{V} \sum_{\mathbf{k}, \lambda} \delta(\omega - ck) \quad (\text{S16})$$

where  $V = L^3$ . Using the limit where  $L \rightarrow \infty$  and

$$\frac{1}{V} \sum_{\mathbf{k}} \rightarrow \frac{1}{(2\pi)^3} \int d^3 k, \quad (\text{S17})$$

we obtain the free space photon DOS using standard manipulations

$$D_0(\omega) = 2 \frac{4\pi}{(2\pi)^3} \cdot \frac{\omega^2}{c^3} = \frac{\omega^2}{\pi^2 c^3}. \quad (\text{S18})$$

The energy density  $\rho_0(\omega, T)$  of free-field blackbody radiation can be obtained by multiplying the density of states with the Bose-Einstein distribution function and the energy of each photon:

$$\rho_0(\omega, T) = D_0(\omega) n(\omega, T) = \frac{\omega^2}{\pi^2 c^3} \cdot \frac{\hbar \omega}{e^{\frac{\hbar \omega}{k_B T}} - 1}. \quad (\text{S19})$$

#### S4. Empty microcavity thermal radiation

Consider an optical Fabry-Perot microcavity composed of two parallel perfect mirrors with area  $S$  separated by a distance  $L$ . The microcavity mode frequencies are given by

$$\omega_C(m, q) = c\sqrt{q_x^2 + q_y^2 + \left(\frac{m\pi}{L}\right)^2}, \quad (\text{S20})$$

where  $\mathbf{q} = (q_x, q_y)$  is the in-plane wave vector (momentum) corresponding to the in-plane momentum of the cavity modes, and  $m$  is zero (transverse magnetic polarization only) or a positive integer (for transverse electric and transverse magnetic modes) representing the quantization of the wavevector in the  $z$ -direction (perpendicular to the mirror planes) [18, 19]. It follows the empty microcavity DOS is given by

$$D_C(\omega) = \frac{1}{V} \sum_{m, \mathbf{q}, \lambda} \delta[\omega - \omega_C(m, q)], \quad (\text{S21})$$

where  $V = LS$  is the resonator volume,  $\lambda$  denotes the polarization state, and  $m$  and  $\mathbf{q}$  are as discussed above.

Using standard manipulations, we can write the total density of microcavity photon states as [17]

$$D_C(\omega) = \frac{\omega}{\pi c^2 L} \left\lfloor \frac{\omega L}{\pi c} \right\rfloor + \frac{\omega}{2\pi c^2 L}, \quad (\text{S22})$$

where  $\lfloor x \rfloor$  equals the greatest integer less than or equal to  $x$ . It follows the microcavity blackbody radiation energy density  $\rho_C(\omega, T)$  is

$$\rho_C(\omega, T) = D_C(\omega)n(\omega, T) = \frac{\left\{ \left\lfloor \frac{\omega L}{\pi c} \right\rfloor + \frac{1}{2} \right\} \omega}{\pi c^2 L} \frac{\hbar\omega}{e^{\frac{\hbar\omega}{k_B T}} - 1}. \quad (\text{S23})$$

### S5. Microcavity thermal radiation and density of states under strong light-matter coupling

In the strong coupling regime, the Hamiltonian of the system is the sum of the Hamiltonians of the matter, field, and the matter-field interaction:

$$H_{\text{tot}} = H_L + H_M + H_{\text{INT}}, \quad (\text{S24})$$

where each term is defined as follows: The free photon field Hamiltonian is

$$H_L = \sum_{\mathbf{q}, m, \lambda} \hbar \omega_C(m, q) \left( a_{m\mathbf{q}\lambda}^\dagger a_{m\mathbf{q}\lambda} + \frac{1}{2} \right) \quad (\text{S25})$$

with in-plane wavevector  $\mathbf{q} = (q_x, q_y)$ , the mode number  $m$ , and the polarization index  $\lambda$  defined in Eqs. S20, S21. The matter Hamiltonian describes a homogeneous dispersionless isotropic material ensemble with significant infrared oscillator strength at a suitable frequency  $\omega_M$  with effective Hamiltonian [20]:

$$H_M = \int_{D_M} \frac{d^3r}{v} \left[ \frac{\boldsymbol{\pi}^2(\mathbf{r})}{2m^*} + \frac{m^* \omega_M^2 \phi^2(\mathbf{r})}{2} \right], \quad (\text{S26})$$

where  $D_M$  is the region of space occupied by the material,  $v$  is the volume occupied by a single local oscillator (“unit-cell volume”),  $m^*$  is the effective mass,  $\mathbf{r} = (x, y, z) \in D_M$  and  $\boldsymbol{\pi}(\mathbf{r})$  and  $\phi(\mathbf{r})$  represent the conjugate momentum and the matter displacement field respectively. The latter can be rewritten as:

$$\phi(\mathbf{r}) = \sqrt{\frac{\hbar}{2m^* N \omega_M}} \sum_{\mathbf{q}, m, \lambda} \left[ b_{m\mathbf{q}\lambda} \mathbf{u}_{m\mathbf{q}\lambda}(\mathbf{r}) e^{i\mathbf{q}\cdot\mathbf{r}_{\parallel}} + b_{m\mathbf{q}\lambda}^\dagger \mathbf{u}_{m\mathbf{q}\lambda}^*(\mathbf{r}) e^{-i\mathbf{q}\cdot\mathbf{r}_{\parallel}} \right], \quad (\text{S27})$$

where  $b_{m\mathbf{q}\lambda}$  and  $b_{m\mathbf{q}\lambda}^\dagger$  are the annihilation and creation operators for the collective matter excitation labeled by  $(m\mathbf{q}\lambda)$ ,  $N = S/v$  denotes the number of molecular modes per unit length,  $\mathbf{u}_{m\mathbf{q}\lambda}(\mathbf{r})$  is the mode spatial profile vector and  $\mathbf{r}_{\parallel} = (x, y)$ . Each local oscillator vibration is triply degenerate. The excitations can be treated as bosonic following the standard dilute excitation limit. In this case, the Hamiltonian can be written in a simple way using second-quantization

$$H_M = \sum_{\mathbf{q}, m, \lambda} \hbar \omega_M b_{m\mathbf{q}\lambda}^\dagger b_{m\mathbf{q}\lambda}. \quad (\text{S28})$$

We work in the dipole gauge, where the light-matter interaction is given by

$$H_{\text{int}} = \frac{1}{2\epsilon_0} \int_{D_M} [-2\mathbf{D}(\mathbf{r}) \cdot \mathbf{P}(\mathbf{r}) + \mathbf{P}^2(\mathbf{r})] d^3\mathbf{r}, \quad (\text{S29})$$

where  $\mathbf{P}(\mathbf{r})$  is the matter polarization density given by:

$$\mathbf{P}(\mathbf{r}) = \frac{eZ^* \phi(\mathbf{r})}{v}, \quad (\text{S30})$$

where  $eZ^*$  is the effective charge, and  $\mathbf{D}(\mathbf{r})$  is the electrical displacement field [21, 22]

$$\mathbf{D}(\mathbf{r}) = \sum_{\mathbf{q}, m, \lambda} \sqrt{\frac{\epsilon_0 \hbar \omega_C(m, q)}{2V}} \left( \mathbf{u}_{m\mathbf{q}\lambda}(\mathbf{r}) a_{m\mathbf{q}\lambda} e^{i\mathbf{q}\cdot\mathbf{r}_{\parallel}} - \mathbf{u}_{m\mathbf{q}\lambda}^*(\mathbf{r}) a_{-m\mathbf{q}\lambda}^\dagger e^{-i\mathbf{q}\cdot\mathbf{r}_{\parallel}} \right), \quad (\text{S31})$$

and  $V = SL_C$  is the microcavity volume. Inserting the polarization operator expression in second-quantization representation into the light-matter interaction and separately writing linear and quadratic terms of the interaction Hamiltonian in the matter polarization field[23] we obtain

$$H_{\text{int},1} = i \sum_{\mathbf{q},m,\lambda} \frac{\hbar\Omega_R}{2} \sqrt{\frac{\omega_C(m,q)}{\omega_M}} \left( a_{m\mathbf{q}\lambda}^\dagger - a_{-m\mathbf{q}\lambda} \right) \left( b_{m\mathbf{q}\lambda} + b_{-m\mathbf{q}\lambda}^\dagger \right), \quad (\text{S32})$$

$$H_{\text{int},2} = \sum_{\mathbf{q},m,\lambda} \hbar\omega_M b_{m\mathbf{q}\lambda}^\dagger b_{m\mathbf{q}\lambda} + \frac{\hbar\Omega_R^2}{4\omega_M} \left( b_{m\mathbf{q}\lambda}^\dagger + b_{m-\mathbf{q}\lambda} \right) \left( b_{m-\mathbf{q}\lambda}^\dagger + b_{m\mathbf{q}\lambda} \right) \quad (\text{S33})$$

where  $\Omega_R = \sqrt{\frac{(eZ^*)^2}{\epsilon_0 m^* v}}$  is the coupling constant, describing the strength of the interaction between the light field and the molecular excitations. To find the normal modes of the light-matter system, we first define a new set of operators  $p_{m\mathbf{q}\lambda}$  such that:

$$[p_{m\mathbf{q}\lambda}, H_M + H_{\text{int},2}] = \hbar\Omega_M p_{m\mathbf{q}\lambda}, \quad \Omega_M^2 = \omega_M^2 + \Omega_R^2 \quad (\text{S34})$$

where  $\Omega_M$  represents the renormalized material excitation due to light-matter coupling inside the microcavity. The new polarization operators  $p_{m\mathbf{q}\lambda}$  are written in terms of the original matter operators  $b_{m\mathbf{q}\lambda}$  and their conjugates:

$$p_{m\mathbf{q}\lambda} = \frac{\Omega_M + \omega_M}{2\sqrt{\Omega_M\omega_M}} b_{m\mathbf{q}\lambda} + \frac{\Omega_M - \omega_M}{2\sqrt{\Omega_M\omega_M}} b_{m-\mathbf{q}\lambda}^\dagger. \quad (\text{S35})$$

This transformation effectively diagonalizes the quadratic part of the Hamiltonian, allowing us to describe the system in terms of new quasi-particles that reflect the modified nature of the molecular excitations under strong coupling. The total Hamiltonian, now expressed in terms of the new operators, takes the form:

$$\begin{aligned} H_{\text{total}} = & \sum_{\mathbf{q},m,\lambda} \hbar\Omega_M p_{m\mathbf{q}\lambda}^\dagger p_{m\mathbf{q}\lambda} + \sum_{\mathbf{q},m,\lambda} \hbar\omega_C(m,q) \left( a_{m\mathbf{q}\lambda}^\dagger a_{m\mathbf{q}\lambda} + \frac{1}{2} \right) \\ & + i \sum_{\mathbf{q},m,\lambda} \hbar \frac{\Omega_R}{2} \sqrt{\frac{\omega_C(m,q)}{\Omega_M}} \left( a_{m\mathbf{q}\lambda}^\dagger - a_{-m\mathbf{q}\lambda} \right) \left( p_{m\mathbf{q}\lambda} + p_{-m\mathbf{q}\lambda}^\dagger \right), \end{aligned} \quad (\text{S36})$$

To obtain the polaritonic (hybrid) normal-modes after performing this initial matter Bogoliubov transformations, we note the total light-matter Hamiltonian can be written as:

$$H_{\text{total}} = \sum_{\mathbf{q},m,\lambda} \hbar\omega(m,q) \Pi_{m\mathbf{q}\lambda}^\dagger \Pi_{m\mathbf{q}\lambda}, \quad (\text{S37})$$

where  $\Pi_{m\mathbf{q}\lambda}^\dagger$  and  $\Pi_{m\mathbf{q}\lambda}$  are the creation and annihilation operators of polariton modes. In what follows, we simplify the notation by replacing  $m\mathbf{q}\lambda$  in polariton operators by  $k$ . Polariton annihilation operators are given by

$$\Pi_k = x_k a_k + y_k a_{-k}^\dagger + z_k p_k + t_k p_{-k}^\dagger. \quad (\text{S38})$$

where  $x_k$  and  $y_k$  are the Hopfield coefficients representing the photonic contributions, and  $z_k$  and  $t_k$  are the coefficients representing the matter contributions. These coefficients are obtained by enforcing the bosonic commutation relations for the polariton operators and the condition  $[\Pi_k, H_{\text{tot}}] = \hbar\omega(k)\Pi_k$  where  $\omega(k)$  is a normal-mode (polariton) frequency. This leads to the set of

linear equations.

$$|x_k|^2 - |y_k|^2 + |z_k|^2 - |t_k|^2 = 1, \quad (\text{S39})$$

$$[\omega(k) - \omega_C(m, q)]x_k + G\sqrt{\frac{\omega_C(m, q)}{\Omega_M}}(z_k + t_k) = 0, \quad (\text{S40})$$

$$[\omega(k) + \omega_C(m, q)]y_k + G\sqrt{\frac{\omega_C(m, q)}{\Omega_M}}(z_k + t_k) = 0, \quad (\text{S41})$$

$$[\omega(k) - \Omega_M]z_k - G\sqrt{\frac{\omega_C(m, q)}{\Omega_M}}(x_k - y_k) = 0, \quad (\text{S42})$$

$$[\omega(k) + \Omega_M]t_k + G\sqrt{\frac{\omega_C(m, q)}{\Omega_M}}(x_k - y_k) = 0, \quad (\text{S43})$$

where  $\omega_C(m, \mathbf{q})$  is the cavity mode frequency, and  $G = \frac{i\hbar\Omega_R}{2}$  is the light-matter coupling constant. These equations can be used to find the polariton frequencies as the solutions to

$$[\omega^2(k) - \Omega_M^2][\omega^2(k) - \omega_C^2(m, q)] - \Omega_R^2\omega_C^2(m, q) = 0. \quad (\text{S44})$$

Specifically, the polariton frequencies  $\omega_{\pm}(k)$  are given by

$$\omega_{\pm}^2(k) = \frac{1}{2} \left[ \omega_C^2(m, q) + \omega_M^2 + \Omega_R^2 \pm \sqrt{[\omega_M^2 + \Omega_R^2 - \omega_C^2(m, q)]^2 + 4\omega_C^2(m, q)\Omega_R^2} \right]. \quad (\text{S45})$$

Substituting the expressions for  $x_k$  and  $z_k$  into Eq. S39, we get:

$$y_k = \frac{[\omega(k) - \omega_C(m, q)][\omega^2(k) - \Omega_M^2]}{2\sqrt{\omega(k)\omega_C(m, q)}\sqrt{[\omega^2(k) - \Omega_M^2]^2 + \Omega_R^2\omega_C^2(m, q)}}, \quad (\text{S46})$$

$$x_k = \frac{[\omega(k) + \omega_C(m, q)][\omega^2(k) - \Omega_M^2]}{2\sqrt{\omega(k)\omega_C(m, q)}\sqrt{[\omega^2(k) - \Omega_M^2]^2 + \Omega_R^2\omega_C^2(m, q)}}. \quad (\text{S47})$$

We can rewrite the photon and the matter field operators in terms of the polaritonic operators

$$a_k = x_k^* \Pi_k - y_k \Pi_{-k}^\dagger, \quad (\text{S48})$$

$$p_k = z_k^* \Pi_k - t_k \Pi_{-k}^\dagger. \quad (\text{S49})$$

The photonic part of each polariton mode  $k = (m, \mathbf{q}, \lambda)$  with frequency  $\omega$  is given by  $P_C(\omega) = |x_k|^2 - |y_k|^2$  and matter part is  $P_M(\omega) = |z_k|^2 - |t_k|^2$  [23]. In terms of the matter and photon frequencies and the collective light-matter coupling strength,  $P_C(\omega)$  is given by

$$P_C(\omega) = \frac{(\omega^2 - \omega_M^2 - \Omega_R^2)^2}{(\omega^2 - \omega_M^2 - \Omega_R^2)^2 + \omega_C^2(\omega)\Omega_R^2}, \quad (\text{S50})$$

where  $\omega_C(\omega)$  is the frequency of the photon mode that hybridizes with matter polarization to give a polariton mode with frequency  $\omega$  (Eq. S45). The group velocity  $v_g(\omega, q)$  of a polariton with frequency  $\omega$  and in-plane wave vector magnitude  $q$  can be

obtained by taking the derivative of Eq. S45 with respect to  $q$

$$v_g(\omega, q) = \frac{d\omega_{\pm}}{dq} = \frac{qc^2}{2\omega} \left( 1 \pm \frac{\omega_C^2 - \omega_M^2 + \Omega_R^2}{\sqrt{[\omega_C^2 + \omega_M^2 + \Omega_R^2]^2 - 4\omega_C^2(\omega)\omega_M^2}} \right), \quad (\text{S51})$$

where we take the positive sign if the polariton mode with frequency  $\omega$  is in a UP branch [if  $\omega > \omega_C(\omega)$ ] and the negative sign otherwise. The previous results will be employed to obtain the polariton density of states  $D(\omega)$  defined as

$$D(\omega) = \frac{1}{V} \sum_{\mathbf{q}, m, \lambda, \alpha = \pm} \delta[\omega - \omega_{\alpha}(m, q)]. \quad (\text{S52})$$

We obtain a closed-form expression of the polariton density of states by using

$$\delta[\omega - \omega_{\alpha}(m, q)] = \frac{\delta[q - q(m, \omega_{\alpha})]}{v_g[\omega, q(m, \omega)]} \quad (\text{S53})$$

where  $q(m, \omega)$  is the in-plane wave vector magnitude that corresponds to the polariton frequency  $\omega = \omega_{\alpha}(m, q)$  for a given mode order  $m$  and polarization  $\lambda$ . Substituting this result into Eq. S52 and integrating over the space of in-plane wave vectors, we obtain

$$D(\omega) = \frac{1}{L_C} \sum_{m, \lambda} \frac{q(m, \omega)}{2\pi} \frac{1}{v_g(\omega, q)} \theta[\omega_C(\omega) - m\pi c/L_C] \quad (\text{S54})$$

where  $\theta[.]$  is the Heaviside step function. The rate of spontaneous emission of a material system under weak coupling with the electromagnetic field of a polaritonic device is controlled by the photon-weighted polariton DOS (PDOS)

$$D_P(\omega) = P_C(\omega)D(\omega) \quad (\text{S55})$$

$$= \frac{1}{L_C} \sum_{m, \lambda} \frac{q(m, \omega)P_C(\omega)}{2\pi v_g(\omega, q)} \theta[\omega_C(\omega) - m\pi c/L_C]. \quad (\text{S56})$$

This quantity can be split into the sum of a contribution from  $m = 0$  and  $m > 0$ . For  $m = 0$ , there is only TM<sub>0</sub> mode contribution, but for  $m > 0$ , there are both TE and TM modes, resulting in a factor of 2 for the polarization sum. It follows that the PDOS can be written as:

$$D_P(\omega) = \frac{1}{L_C} \sum_{m>0} \frac{q(m, \omega)P_C(\omega)}{\pi v_g(\omega, q)} \theta[\omega_C - m\pi c/L] + \frac{q_0(\omega)P_C(\omega)}{2\pi L_C v_g[\omega, q_0(\omega)]}, \quad (\text{S57})$$

where  $q_0(\omega) = q(m = 0, \omega)$ . This expression for  $D_P(\omega)$  can be written as a single sum by denoting polariton frequencies by  $\omega$  and writing

$$D_P(\omega) = \sum_{m=0}^{\infty} \left( 1 - \frac{\delta_{0,m}}{2} \right) \frac{q(m, \omega)P_C(\omega)}{\pi v_g[\omega, q(m, \omega)]L_C} \theta[\omega_C(\omega) - m\pi c/L_C]. \quad (\text{S58})$$

The thermal radiation energy density  $\rho_P(\omega, T)$  in a polaritonic system can be written as the product of the polariton energy, the Bose-Einstein distribution, and the photon-weighted polariton density of states

$$\rho_P(\omega, T) = D_P(\omega) \frac{\hbar\omega}{e^{\frac{\hbar\omega}{k_B T}} - 1}. \quad (\text{S59})$$

Substituting the expression for  $D_P(\omega)$ , we obtain:

$$\rho_P(\omega, T) = \sum_{m=0}^{\infty} \left(1 - \frac{\delta_{0,m}}{2}\right) \frac{q(m, \omega) P_C(\omega)}{\pi v_g[\omega, q(m, \omega)] L_C} \frac{\hbar\omega}{e^{\frac{\hbar\omega}{k_B T}} - 1} \theta[\omega_C(\omega) - m\pi c/L_C]. \quad (\text{S60})$$

This expression can be used to calculate the contribution of polaritonic modes to the overall thermal radiation inside a micro-cavity, considering both the upper and lower polariton branches. Equation S60 is particularly useful for computing the thermal absorption and emission rates of a charged system weakly coupled to a polaritonic material.

## S6. Sensitivity Analysis

Due to the modified DOS, microcavities may enhance or suppress multiple vibrational transitions (relative to free space) in both weak and strong coupling regimes. We performed a sensitivity analysis to find which transitions are the most impactful to the BIRD rate. This consists of the following procedure for each fundamental or overtone transition frequency  $\omega_{ij}$ .

We perturb the free space photon DOS at  $\omega_{ij}$  by scaling this quantity by a factor of  $f$

$$D_0(\omega_{ij}) \rightarrow f \cdot D_0(\omega_{ij}). \quad (\text{S61})$$

Since transition rates are proportional to the DOS, the transitions associated with the absorption or emission of photons with frequency  $\omega_{ij}$  are effectively scaled by the same factor, while all other transitions remain with free space rates. The corresponding perturbed transition matrix,  $\mathbf{J}$  is then constructed, and from its lowest eigenvalue, a perturbed BIRD rate is obtained and assigned a sensitivity score  $S_{ij}$  based on the definition

$$S_{ij} = \frac{\text{free space BIRD rate after perturbation}}{\text{free space BIRD rate with no perturbation}} - 1. \quad (\text{S62})$$

Repeating this procedure for all  $i \neq j$  combinations yields a sensitivity matrix  $\mathbf{S}$  shown as a heat map in Fig. S3. The  $\mathbf{S}$  matrix is symmetric given that emission and absorption depend on the photon DOS at the same frequency, i.e., it is impossible to enhance/suppress one process without also affecting the reverse process.

From Fig. S3, we see that for both HF and LiH, the most important transitions are overtones that reach the final bound state from relatively high energy vibrational levels ( $i \rightarrow 23$  for HF and  $i \rightarrow 29$  for LiH). We list these transitions, along with their energies and sensitivity scores in Tables S3 and S4. The fact that these overtones dominate the dissociation dynamics may be understood from the observation that, in anharmonic systems, fundamental transitions  $i \rightarrow i \pm 1$  are increasingly slowed as we climb the energy level ladder. For example, in the LiH case, fundamental transitions starting at  $n = 25$  involve energies under  $200 \text{ cm}^{-1}$ . Such transitions have, in general, weak oscillator strength and correspond to small DOS and thermal photon populations. Hence, overtones play a dominant role at these higher energy levels and act as bottlenecks for dissociation from the highest energy-bound state.

TABLE S3. Most important transitions according to their sensitivity analysis score for HF.

Transition	Energy ( $\text{cm}^{-1}$ )	Sensitivity ( $\delta = 1.5$ )	Sensitivity ( $\delta = 0.5$ )
16 $\rightarrow$ 23	4690.0	0.109	-0.110
15 $\rightarrow$ 23	6053.6	0.102	-0.102
14 $\rightarrow$ 23	7590.6	0.064	-0.064
20 $\rightarrow$ 23	969.6	0.057	-0.057
17 $\rightarrow$ 23	3499.8	0.051	-0.051
19 $\rightarrow$ 23	1639.6	0.043	-0.043
13 $\rightarrow$ 23	9301.0	0.032	-0.032
21 $\rightarrow$ 23	473.0	0.017	-0.017
12 $\rightarrow$ 23	11184.8	0.013	-0.013
11 $\rightarrow$ 23	13242.0	0.005	-0.005

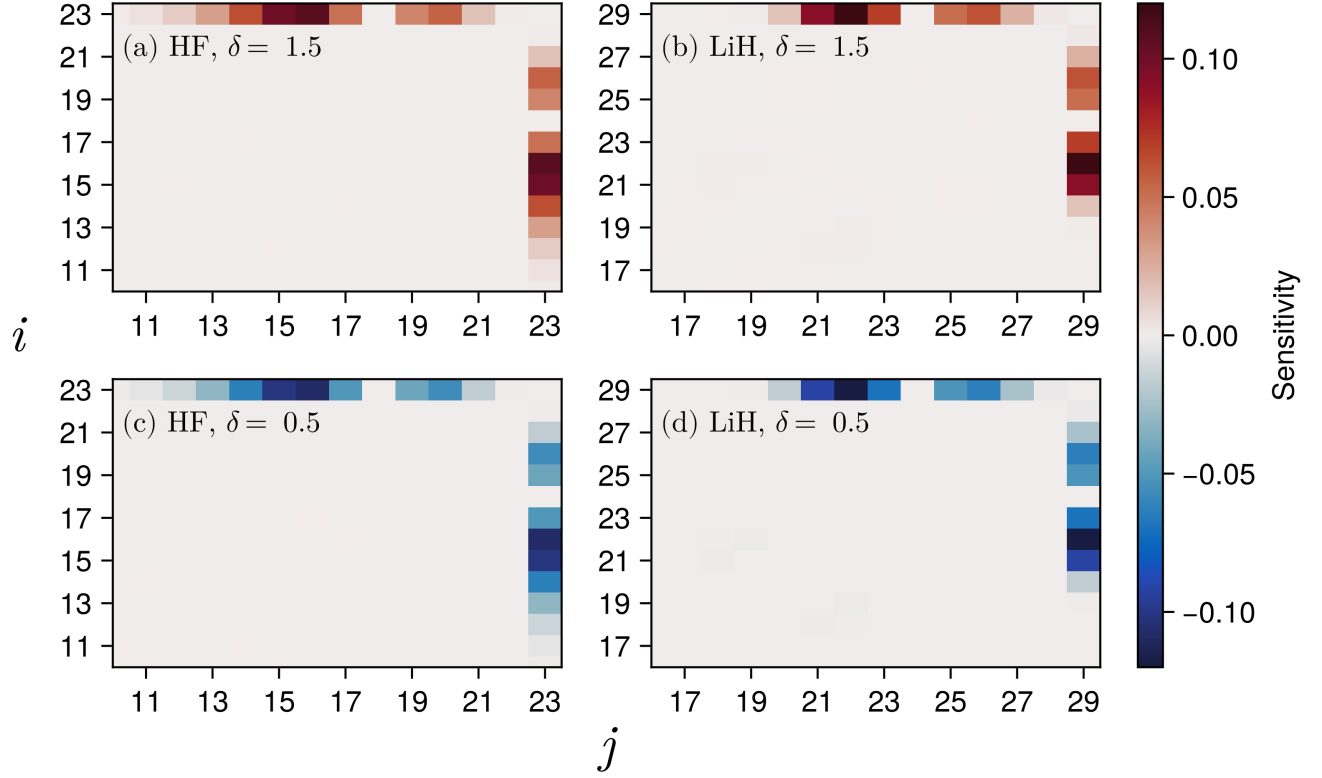


FIG. S3. Sensitivity analysis for both HF and LiH under enhancement ( $\delta = 1.5$ ) and suppression ( $\delta = 0.5$ ). The sensitivity was calculated using Eq. S62 following the procedure described in this section. Transitions not shown in the plot have negligible sensitivity.

TABLE S4. Most important transitions according to their sensitivity analysis score for LiH.

Transition	Energy ( $\text{cm}^{-1}$ )	Sensitivity ( $\delta = 1.5$ )	Sensitivity ( $\delta = 0.5$ )
22 $\rightarrow$ 29	1401.9	0.157	-0.160
21 $\rightarrow$ 29	1787.5	0.092	-0.093
23 $\rightarrow$ 29	1062.6	0.070	-0.071
26 $\rightarrow$ 29	322.8	0.063	-0.064
25 $\rightarrow$ 29	523.1	0.052	-0.053
27 $\rightarrow$ 29	168.9	0.024	-0.025
20 $\rightarrow$ 29	2219.4	0.017	-0.017
28 $\rightarrow$ 29	61.3	0.003	-0.003
19 $\rightarrow$ 22	1295.8	0.001	-0.002
19 $\rightarrow$ 29	2697.7	0.001	-0.001

Temperature (K)	$k_0$ (s <sup>-1</sup> )	$k_c$ (s <sup>-1</sup> )	$k_p$ (s <sup>-1</sup> )
1000	$5.96 \times 10^{-12}$	$6.39 \times 10^{-12}$	$3.26 \times 10^{-10}$
1500	$1.18 \times 10^{-7}$	$1.27 \times 10^{-7}$	$3.33 \times 10^{-6}$
2000	$1.64 \times 10^{-5}$	$1.78 \times 10^{-5}$	$3.14 \times 10^{-4}$
2500	$3.15 \times 10^{-4}$	$3.42 \times 10^{-4}$	$4.56 \times 10^{-3}$
3000	$2.23 \times 10^{-3}$	$2.43 \times 10^{-3}$	$2.58 \times 10^{-2}$

TABLE S5. Absolute BIRD rates for LiH in free space ( $k_0$ ), weak coupling regime ( $k_c$ ), and strong coupling regime ( $k_p$ ). In all cases,  $L_C = 9.6 \mu\text{m}$ ,  $\Omega_R = 200 \text{ cm}^{-1}$ , and  $\omega_M = 1402 \text{ cm}^{-1}$ .

### S7. Temperature Dependence

Diatomic molecules such as HF and LiH are bound by a strong covalent bond that is stable even at temperatures much higher than room temperature. This means their dissociation from the most energetic bound state by thermal radiation can only happen at very high temperatures. In this section, we discuss the temperature dependence of the reported relative rates and demonstrate that the qualitative analysis presented in the main manuscript holds for all examined temperatures.

Achieving numerically stable BIRD rate constants (lowest eigenvalue of transition matrix  $\mathbf{J}$ ) is straightforward at sufficiently high temperatures (e.g., comparable to or larger than the vibrational temperatures of the modeled diatomics). At such temperatures (e.g., 2000 K for LiH and 4000 K HF), the rate constants for absorption and emission are large enough that floating point arithmetic errors are negligible. In Fig. S4, we present relative BIRD rates for temperatures as low as 1000 K in weak and strong coupling regimes. To mitigate floating point errors, these computations were performed using quadruple precision (FLOAT128).

In the main text, we explain that a small change in the cavity length (9.4 to 9.6  $\mu\text{m}$ ) leads to a measurable change in the LiH dissociation rate ( $k_c/k_0$  shifts from 0.93 to 1.09). In Fig. S4(a), this observation remains valid for a large range of temperatures. Although at lower temperatures the enhancement (at  $L_C = 9.6 \mu\text{m}$ ) is smaller, the suppression effect ( $L_C = 9.4 \mu\text{m}$ ) is virtually temperature-independent. Moreover, the sudden change in  $k_c/k_0$  between the two examined cavity lengths is still present for all temperatures. This can be explained with the same arguments from Fig. 3 in the main text.

Relative BIRD rates for LiH in the strong coupling regime are shown in Fig. S4(b) for a range of temperatures. Here we present results for two specific values of matter host frequency:  $\omega_M = 1399 \text{ cm}^{-1}$ , which causes the 22  $\rightarrow$  29 overtone to be completely suppressed (See Table S4); and  $\omega_M = 1402 \text{ cm}^{-1}$  where the 22  $\rightarrow$  29 overtone transition rate is greatly enhanced leading to an increased BIRD rate. From Fig. S4 (b), we observe a moderate temperature dependence when  $\omega_M = 1402 \text{ cm}^{-1}$ . However, the qualitative picture remains the same: when  $\omega_M = 1399 \text{ cm}^{-1}$ , the suppression of the 22  $\rightarrow$  29 overtone causes a mild reduction of the BIRD rate, whereas at  $\omega_M = 1402 \text{ cm}^{-1}$ , this overtone transition rate is enhanced and polariton-assisted BIRD via the highest energy bound state is faster by one order of magnitude relative to free space.

Selected numerical values of  $k_0$ ,  $k_c$ , and  $k_p$  are shown in Table S5. Although polariton-assisted enhancements ( $k_p/k_0$ ) become more significant at lower temperatures, Table S5 shows BIRD rates are extremely low at the smallest examined temperatures. For example, at  $T = 1000 \text{ K}$   $k_0$  is on the order of  $O(10^{-12}/\text{s})$ . Hence, we focus our analysis on temperatures comparable to the LiH and HF vibrational temperatures. A more comprehensive examination of thermal effects is left for future work.

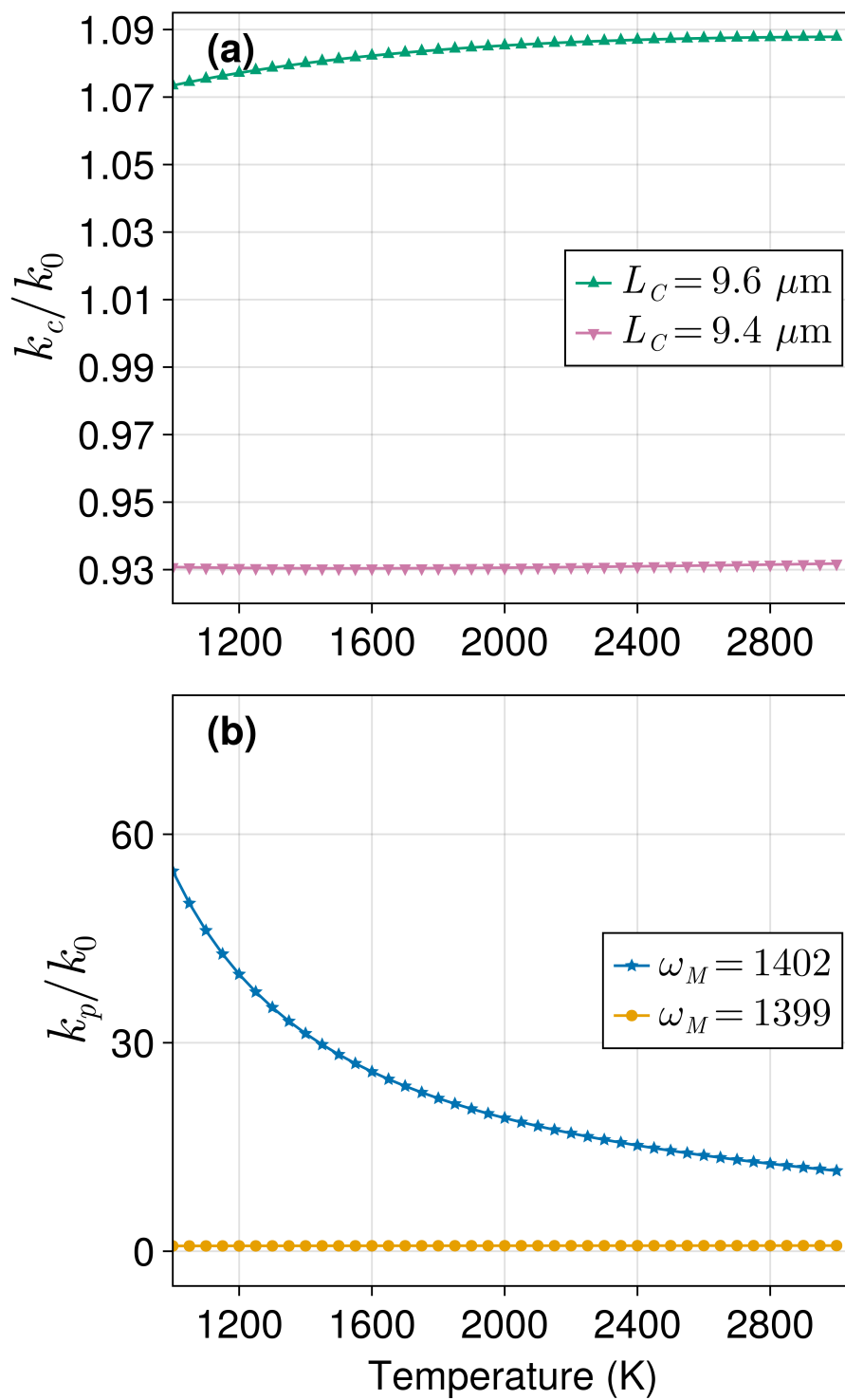


FIG. S4. Temperature dependence of the relative BIRD rates for LiH in the (a) weak and (b) strong coupling regimes. In (b),  $\Omega_R = 200 \text{ cm}^{-1}$  and  $L_C = 9.6 \mu\text{m}$

### S8. Rates without Overtones

The sensitivity analysis in Sec. S6 revealed that specific overtone transitions act as bottlenecks for the investigated diatomic BIRD from the most energetic bound state. In this section, we provide computations in the weak coupling regime that include only transitions between nearest energy levels  $i \rightarrow i \pm 1$  and ignore the effects of overtones. The results are shown in Fig. S5 and Table S6, which show that overtones are essential for accurately capturing the BIRD kinetics inside and outside a microcavity.

Fig. S5 shows relative rates for a range of microcavity lengths in the weak coupling regime. Note that Fig. S5 is similar to Fig. 2 of the main text, but only transitions between neighboring levels are allowed here. The results are qualitatively different. The complicated pattern seen in Fig. 2 is substituted by a much simpler function that can be fully understood by analyzing a single transition. A sensitivity analysis reveals that the most important transitions for HF and LiH are  $22 \rightarrow 23$  and  $28 \rightarrow 29$ , respectively. These transitions correspond to  $i_{\max} - 1 \rightarrow i_{\max}$  and have very small frequencies, 149.8 for HF and  $61.3 \text{ cm}^{-1}$  for LiH. Thus, oscillations in the relative rates ( $k_c/k_0$ ) with changes in microcavity length occur over much larger periods (compare the axes of Fig. 2 and Fig. S5). Dotted green and pink lines in Fig. S5 represent the relative microcavity DOS at 149.8 and  $61.3 \text{ cm}^{-1}$ , demonstrating the effect on the BIRD rate depends only on the photon DOS at the  $i_{\max} - 1 \rightarrow i_{\max}$  transition frequency. Finally, we also emphasize the quantitative effect of neglecting overtones. The free space rates ( $k_0$ ) are reduced by three orders of magnitude when the model includes only fundamental transitions (Table S6).

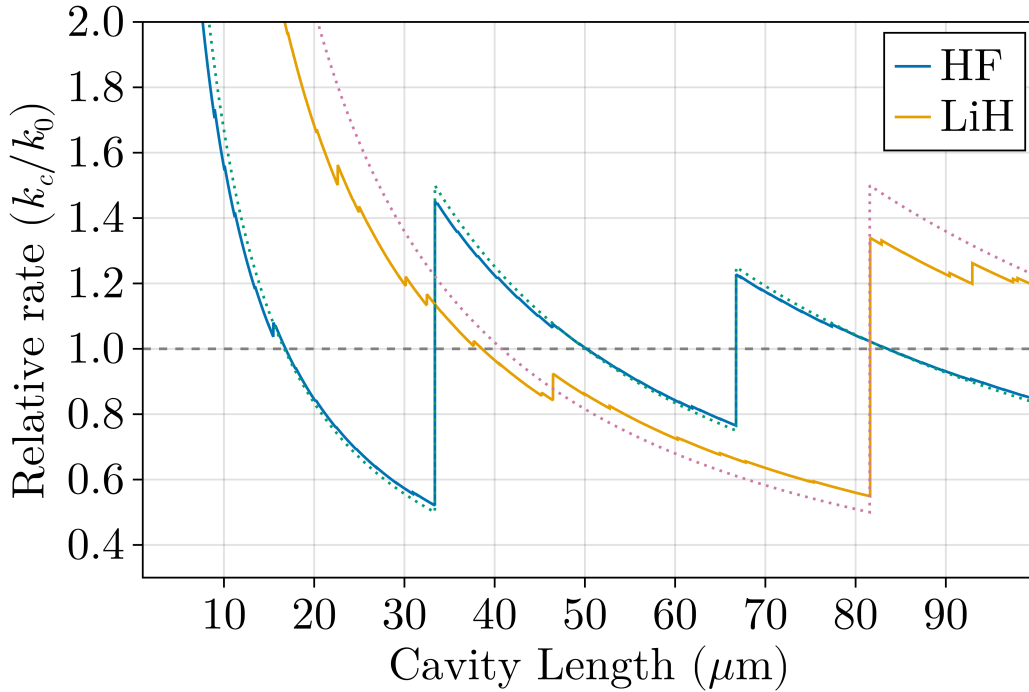


FIG. S5. Ratio of BIRD rate, computed without overtones, inside a microcavity (weak coupling regime) to the free-space rate as a function of microcavity length for HF and LiH molecules. Dotted green and pink lines represent the relative density of states,  $D_C(\omega)/D_0(\omega)$ , at  $\omega = 149.8 \text{ cm}^{-1}$  and  $\omega = 61.3 \text{ cm}^{-1}$ , respectively.

	$k_0$ without overtones ( $\text{s}^{-1}$ )	$k_0$ with overtones ( $\text{s}^{-1}$ )
HF	$5.68 \times 10^{-9}$	$2.70 \times 10^{-6}$
LiH	$7.73 \times 10^{-8}$	$1.64 \times 10^{-5}$

TABLE S6. Computed free space BIRD rates ( $k_0$ ) with and without overtone transitions at  $T = 2000$  and  $4000 \text{ K}$  for LiH and HF, respectively.

- 
- [1] J. Stine and D. Noid, Classical treatment of the dissociation of hydrogen fluoride with one and two infrared lasers, *Opt. Commun* **31**, 161–164 (1979).
- [2] A. Guldberg and G. D. Billing, Laser-induced dissociation of hydrogen fluoride, *Chem. Phys. Lett* **186**, 229–237 (1991).
- [3] P. Gross, D. Neuhauser, and H. Rabitz, Teaching lasers to control molecules in the presence of laboratory field uncertainty and measurement imprecision, *J. Chem. Phys.* **98**, 4557–4566 (1993).
- [4] M. Kaluža, J. T. Muckerman, P. Gross, and H. Rabitz, Optimally controlled five-laser infrared multiphoton dissociation of HF, *The Journal of Chemical Physics* **100**, 4211 (1994).
- [5] K. K. Irikura, Experimental vibrational zero-point energies: Diatomic molecules, *JPCRD* **36**, 389–397 (2007).
- [6] W. C. Stwalley and W. T. Zemke, Spectroscopy and structure of the lithium hydride diatomic molecules and ions, *JPCRD* **22**, 87–112 (1993).
- [7] M. Dulick, K.-Q. Zhang, B. Guo, and P. Bernath, Far- and mid-infrared emission spectroscopy of lih and lid, *J. Mol. Spectrosc.* **188**, 14–26 (1998).
- [8] S. Nasiri, T. Shomenov, S. Bubin, and L. Adamowicz, Dissociation energy and the lowest vibrational transition in lih without assuming the non-born–oppenheimer approximation, *Mol. Phys.* **120**, 10.1080/00268976.2022.2147105 (2022).
- [9] F. Holka, P. G. Szalay, J. Fremont, M. Rey, K. A. Peterson, and V. G. Tyuterev, Accurate ab initio determination of the adiabatic potential energy function and the born–oppenheimer breakdown corrections for the electronic ground state of lih isotopologues, *J. Chem. Phys.* **134**, 10.1063/1.3555758 (2011).
- [10] W.-C. Tung, M. Pavanello, and L. Adamowicz, Very accurate potential energy curve of the lih molecule, *J. Chem. Phys.* **134**, 10.1063/1.3554211 (2011).
- [11] J. P. Dahl and M. Springborg, The morse oscillator in position space, momentum space, and phase space, *J. Chem. Phys.* **88**, 4535–4547 (1988).
- [12] D. G. A. Smith, L. A. Burns, A. C. Simmonett, R. M. Parrish, M. C. Schieber, R. Galvelis, P. Kraus, H. Kruse, R. Di Remigio, A. Ale-naizan, A. M. James, S. Lehtola, J. P. Misiewicz, M. Scheurer, R. A. Shaw, J. B. Schriber, Y. Xie, Z. L. Glick, D. A. Sirianni, J. S. O’Brien, J. M. Waldrop, A. Kumar, E. G. Hohenstein, B. P. Pritchard, B. R. Brooks, H. F. Schaefer, A. Y. Sokolov, K. Patkowski, A. E. DePrince, U. Bozkaya, R. A. King, F. A. Evangelista, J. M. Turney, T. D. Crawford, and C. D. Sherrill, Psi4 1.4: Open-source software for high-throughput quantum chemistry, *J. Chem. Phys.* **152**, 10.1063/5.0006002 (2020).
- [13] R. C. Dunbar, Bird (blackbody infrared radiative dissociation): evolution, principles, and applications, *Mass spectrometry reviews* **23**, 127 (2004).
- [14] W. G. Valance and E. W. Schlag, Theoretical rate constant for thermal unimolecular reactions in a multilevel system, *The Journal of Chemical Physics* **45**, 216 (1966).
- [15] R. G. Gilbert and S. C. Smith, *Theory of Unimolecular and Recombination Reactions* (Blackwell Scientific Publications, Oxford, UK, 1990).
- [16] P. Hänggi, P. Talkner, and M. Borkovec, Reaction-rate theory: fifty years after kramers, *Rev. Mod. Phys.* **62**, 251 (1990).
- [17] W. L. Barnes, S. A. R. Horsley, and W. L. Vos, Classical antennas, quantum emitters, and densities of optical states, *J. Opt.* **22**, 073501 (2020).
- [18] H. Zoubi and G. La Rocca, Microscopic theory of anisotropic organic cavity exciton polaritons, *Physical Review B* **71**, 235316 (2005).
- [19] J. D. Jackson, *Classical electrodynamics* (John Wiley & Sons, 2021).
- [20] Y. Ashida, A. İmamoğlu, J. Faist, D. Jaksch, A. Cavalleri, and E. Demler, Quantum electrodynamic control of matter: Cavity-enhanced ferroelectric phase transition, *Physical Review X* **10**, 041027 (2020).
- [21] D. Craig and T. Thirunamachandran, *Molecular Quantum Electrodynamics: An Introduction to Radiation-molecule Interactions*, Dover Books on Chemistry Series (Dover Publications, 1998).
- [22] E. A. Power and T. Thirunamachandran, Quantum electrodynamics in a cavity, *Physical Review A* **25**, 2473 (1982).
- [23] Y. Todorov and C. Sirtori, Intersubband polaritons in the electrical dipole gauge, *Physical Review B* **85**, 045304 (2012).